

# Optical Sytem Analysis for the Ground-Based Experimental Vector Magnetograph (EXVM)

Final Report  
6/30/93

Prepared for:

NASA Marshall Space Flight Center  
Contract No. NAS8-38609  
Delivery Order 46

Prepared by:

Dr. L. W. Hillman  
Dr. R. A. Chipman  
M. H. Smith

Department of Physics  
University of Alabama in Huntsville

(NASA-CR-192588) OPTICAL SYSTEM  
ANALYSIS FOR THE GROUND BASED EXVM  
Final Report (Alabama Univ.) 88 p

N93-31035

Unclas

G3/74 0176968

## ABSTRACT

The Marshall Space Flight Center's Experimental Vector Magnetograph (EXVM) is an instrument that observes a  $4.4 \times 8.8$  arcmin field of the sun. The transverse and longitudinal components of the surface magnetic field and the line-of-sight velocities of the photospheric gases can be determined from polarimetric and spectral analysis of the 525.02 nm absorption line of Fe I. The EXVM has been breadboarded and tested in the laboratory. The optics of the EXVM were tested with a point-diffraction (Smartt) interferometer. The 12 inch Cassegrain telescope was found to have 0.20 waves RMS (at 525.02 nm) of aberration. The post-telescope relay optics were nearly diffraction limited on-axis and had about one wave of primary coma as the predominant aberration at full-field. From theoretical modulation transfer function (MTF) curves of known aberrations, it was concluded that the EXVM should attain a maximum spatial resolution of about 0.5 arcseconds. A resolution test target indicated maximum angular resolutions better than 0.6 arcsec on-axis and 0.7 arcsec at full-field-of-view. A 28 inch heliostat (sun-tracking mirror) was used to direct sunlight into the lab and into the EXVM. Solar images obtained were limited by atmospheric seeing effects. During brief moments of good seeing, angular resolutions of about 1 arcsecond were realized with the EXVM.

## TABLE OF CONTENTS

|   | Page |
|---|------|
| <b>(1) OPTICAL DESIGN SUMMARY</b>                                   | 1    |
| (1.1) Y- $\bar{Y}$ Diagram  | 1    |
| (1.2) The Optical Invariant   | 9    |
| (1.3) Telescope   | 10   |
| (1.4) Relay Optics  | 10   |
| (1.5) Detectors   | 13   |
| (1.6) Field of View and Image Sizes                                 | 14   |
| (1.7) Beamsplitter Options  | 16   |
| <b>(2) ALIGNMENT OF THE EXVM</b>                                    | 18   |
| (2.1) Relay Optics  | 19   |
| (2.2) Checking for Collimation with a Shearing Plate Interferometer | 24   |
| (2.3) Adding the 12 inch Cassegrain Telescope                       | 27   |
| <b>(3) TESTING THE OPTICAL SYSTEM OF THE EXVM</b>                   | 30   |
| (3.1) Description of the Foucault Knife-Edge Test                   | 31   |
| (3.2) Application of the Foucault Knife-Edge Test                   | 35   |
| (3.3) Description and Theory of the Smartt Interferometer           | 37   |
| (3.4) Application of the Smartt Interferometer                      | 40   |
| (3.5) Analysis of Interferograms of the 12 in. Cassegrain Telescope | 44   |
| (3.6) Analysis of Interferograms of the Relay Optics                | 51   |
| (3.7) Application of the Resolution Test Target                     | 53   |
| (3.8) Resolution Test Target Analysis                               | 55   |
| (3.9) Solar Image   | 56   |
| <b>(4) SUGGESTIONS FOR FUTURE WORK</b>                              | 59   |
| <b>REFERENCES</b>   | 60   |

**APPENDIX A**      CODE V image evaluation of EXVM design

**APPENDIX B**      CODE V data for various correlation-tracker beamsplitter options

## **(1) OPTICAL DESIGN SUMMARY**

The EXVM was assembled as specified in the optical design developed by Daniel J. Reiley and Dr. Russell A. Chipman under NASA contract NAS8-38609 D.O. 01. Table I lists the CODE V surface descriptions. Since only off-the-shelf lenses and mirrors are used in the EXVM, the corresponding part numbers are included in TABLE I. Figure 1 is a drawing of the optical layout. Note that the lenses have been numbered from 1 to 8 in both Fig. 1 and Table I. This numbering scheme will be used throughout this report to help clarify discussion. Table II lists the CODE V specification data (including effective focal length, image size, lens and mirror apertures, etc.).

Appendix A contains CODE V a paraxial ray trace, ray-fan plots, spot diagrams, RMS wavefront deviation, and modulation transfer function (MTF) curves of the EXVM.

### **(1.1) Y- $\bar{Y}$ Diagram**

Figure 2 is the y- $\bar{y}$  diagram of the EXVM. The marginal and chief ray heights at each surface were obtained from the paraxial ray trace in Appendix A. These values were plotted along the vertical and horizontal axes, respectively.

FIGURE 1. Optical layout of the EXVM.

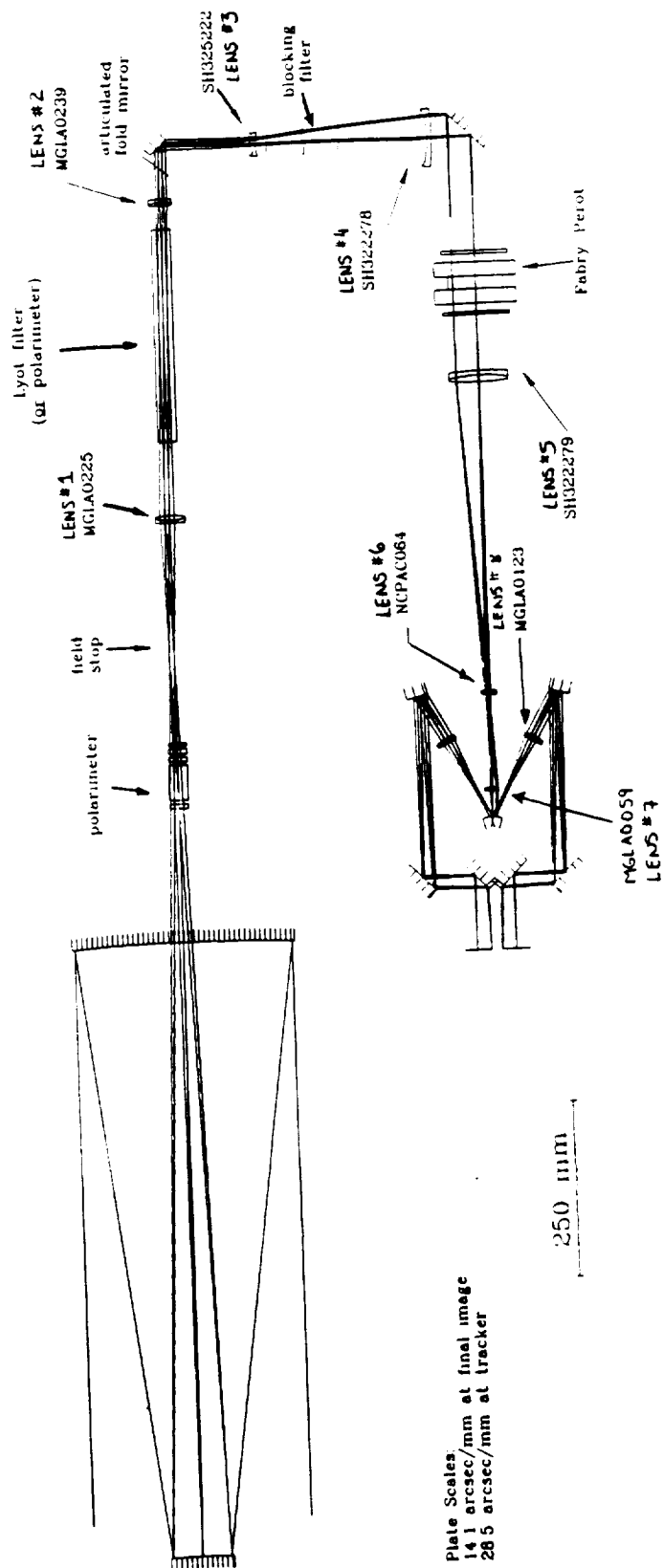


TABLE I. CODE V surface data.

| Surface<br>Number | Radius of<br>Curvature | Thickness   | RMD      | Glass       |   |
|-------------------|------------------------|-------------|----------|-------------|---|
| -----             | -----                  | -----       | ---      | -----       |   |
| > OBJ:            | INFINITY               | INFINITY    |          |             |   |
| 1:                | INFINITY               | 0.001000    |          | BK7_SCHOTT  |   |
| 2:                | INFINITY               | 650.000000  |          |             |   |
| STO:              | -2394.73740            | -877.239800 | REFL     |             | <i>12" Cassegrain Telescope</i>         |
| CON:              |                        |             |          |             |   |
| K :               | -1.000000              | KC :        | 100      |             |   |
| 4:                | -858.24060             | 1069.000000 | REFL     |             |   |
| CON:              |                        |             |          |             |   |
| K :               | -2.825380              | KC :        | 100      |             |   |
| 5:                | INFINITY               | 7.000000    |          | BK7_SCHOTT  |   |
| 6:                | INFINITY               | 5.000000    |          |             |   |
| 7:                | INFINITY               | 50.000000   |          | BK7_SCHOTT  |   |
| 8:                | INFINITY               | 5.000000    |          |             |   |
| 9:                | INFINITY               | 6.000000    |          | BK7_SCHOTT  | <i>Polarimeter</i>                      |
| 10:               | INFINITY               | 5.000000    |          |             |   |
| 11:               | INFINITY               | 7.000000    |          | BK7_SCHOTT  |   |
| 12:               | INFINITY               | 5.000000    |          |             |   |
| 13:               | INFINITY               | 3.000000    |          | BK7_SCHOTT  |   |
| 14:               | INFINITY               | 315.000000  |          |             |   |
| 15:               | 718.39000              | 4.000000    |          | SF8_SCHOTT  |   |
| 16:               | 92.73000               | 6.600000    |          | SSK4_SCHOTT | <i>Lens #1, MGLAO225</i>                |
| 17:               | -128.08000             | 105.000000  |          |             |   |
| 18:               | INFINITY               | 300.000000  |          | BK7_SCHOTT  | <i>Lyot Filter</i>                      |
| 19:               | INFINITY               | 33.500000   |          |             | <i>(alternate polarimeter position)</i> |
| 20:               | 210.75000              | 5.000000    |          | BAK4_SCHOTT |   |
| 21:               | -81.29000              | 4.400000    |          | F3_SCHOTT   | <i>Lens #2, MGLAO239</i>                |
| 22:               | -515.63000             | 75.000000   |          |             |   |
| 23:               | INFINITY               | -128.880000 | REFL     |             |   |
| XDE:              | 0.000000               | YDE:        | 0.000000 | ZDE:        | 0.000000 BEN                            |
| XDC:              | 100                    | YDC:        | 100      | ZDC:        | 100                                     |
| ADE:              | 45.000000              | BDE:        | 0.000000 | CDE:        | 0.000000                                |
| ADC:              | 100                    | BDC:        | 100      | CDC:        | 100                                     |
|                   |                        |             |          |             | <i>Articulated Fold Mirror</i>          |

**TABLE I (cont). CODE V surface data**

|      |            |             |            |                            |      |          |     |
|------|------------|-------------|------------|----------------------------|------|----------|-----|
| 24:  | 141.25000  | -4.800000   | SF5_SCHOTT | Lens #3, SH325222          |      |          |     |
| 25:  | 47.31500   | -3.000000   | BK7_SCHOTT |                            |      |          |     |
| 26:  | -61.74800  | -15.000000  |            |                            |      |          |     |
| 27:  | INFINITY   | 0.010000    | BK7_SCHOTT | Blocking Filters           |      |          |     |
| 28:  | INFINITY   | -48.000000  |            |                            |      |          |     |
| 29:  | INFINITY   | -4.000000   | BK7_SCHOTT |                            |      |          |     |
| 30:  | INFINITY   | -48.000000  |            |                            |      |          |     |
| 31:  | INFINITY   | 0.010000    | BK7_SCHOTT |                            |      |          |     |
| 32:  | INFINITY   | -112.017000 |            |                            |      |          |     |
| 33:  | -188.36000 | -12.500000  | BK7_SCHOTT | Lens #4, SH322278          |      |          |     |
| 34:  | 139.24000  | -6.000000   | SF5_SCHOTT |                            |      |          |     |
| 35:  | 415.67000  | -55.000000  |            |                            |      |          |     |
| 36:  | INFINITY   | 165.233309  | REFL       | Fold Mirror                |      |          |     |
| XDE: | 0.000000   | YDE:        | 0.000000   |                            | ZDE: | 0.000000 | BEN |
| XDC: | 100        | YDC:        | 100        |                            | ZDC: | 100      |     |
| ADE: | 45.000000  | BDE:        | 0.000000   |                            | CDE: | 0.000000 |     |
| ADC: | 100        | BDC:        | 100        |                            | CDC: | 100      |     |
|      |            |             |            |                            |      |          |     |
| 37:  | INFINITY   | 4.000000    | BK7_SCHOTT | Fabry-Pérot Interferometer |      |          |     |
| 38:  | INFINITY   | 12.000000   |            |                            |      |          |     |
| 39:  | INFINITY   | 21.000000   | BK7_SCHOTT |                            |      |          |     |
| 40:  | INFINITY   | 0.000275    |            |                            |      |          |     |
| 41:  | INFINITY   | 18.000000   | BK7_SCHOTT |                            |      |          |     |
| 42:  | INFINITY   | 0.000000    |            |                            |      |          |     |
| 43:  | INFINITY   | 21.000000   | BK7_SCHOTT |                            |      |          |     |
| 44:  | INFINITY   | 12.000000   |            |                            |      |          |     |
| 45:  | INFINITY   | 4.000000    | BK7_SCHOTT |                            |      |          |     |
| 46:  | INFINITY   | 80.000000   |            |                            |      |          |     |
| 47:  | 673.17000  | 6.000000    | SF5_SCHOTT | Lens #5, SH322279          |      |          |     |
| 48:  | 222.27000  | 10.000000   | BK7_SCHOTT |                            |      |          |     |
| 49:  | -302.87000 | 439.000000  |            |                            |      |          |     |
| 50:  | 121.71195  | 3.800000    | BK7_SCHOTT | Lens #6, NCPAC064          |      |          |     |
| 51:  | -89.71796  | 2.500000    | SF5_SCHOTT |                            |      |          |     |
| 52:  | -268.15906 | 131.029506  |            |                            |      |          |     |

**TABLE I (cont). CODE V surface data.**

|      |            |             |             |   |
|------|------------|-------------|-------------|---|
| 53:  | 32.16000   | 4.460000    | SK11_SCHOTT |   |
| 54:  | -22.47000  | 1.500000    | SF5_SCHOTT  | <i>Lens #7, MGLAO059</i>                  |
| 55:  | -89.36000  | 34.925611   |             |   |
| 56:  | INFINITY   | -120.845313 | REFL        |   |
| XDE: | 0.000000   | YDE:        | 0.000000    | ZDE: 0.000000 BEN                         |
| XDC: | 100        | YDC:        | 100         | ZDC: 100                                  |
| ADE: | -15.000000 | BDE:        | 0.000000    | CDE: 0.000000 <i>15° Mirrored Pyramid</i> |
| ADC: | 100        | BDC:        | 100         | CDC: 100                                  |
| 57:  | -182.72000 | -2.000000   | SF5_SCHOTT  |   |
| 58:  | -44.88000  | -4.800000   | SK11_SCHOTT | <i>Lens #8, MGLAO123</i>                  |
| 59:  | 64.04000   | -72.000000  |             |   |
| 60:  | INFINITY   | 257.078523  | REFL        |   |
| XDE: | 0.000000   | YDE:        | 0.000000    | ZDE: 0.000000 BEN                         |
| XDC: | 100        | YDC:        | 100         | ZDC: 100                                  |
| ADE: | 15.000000  | BDE:        | 0.000000    | CDE: 0.000000 <i>Fold Mirror</i>          |
| ADC: | 100        | BDC:        | 100         | CDC: 100                                  |
| 61:  | INFINITY   | -72.000000  | REFL        |   |
| XDE: | 0.000000   | YDE:        | 0.000000    | ZDE: 0.000000 BEN                         |
| XDC: | 100        | YDC:        | 100         | ZDC: 100                                  |
| ADE: | 45.000000  | BDE:        | 0.000000    | CDE: 0.000000 <i>Fold Mirror</i>          |
| ADC: | 100        | BDC:        | 100         | CDC: 100                                  |
| 62:  | INFINITY   | 108.000000  | REFL        |   |
| XDE: | 0.000000   | YDE:        | 0.000000    | ZDE: 0.000000 BEN                         |
| XDC: | 100        | YDC:        | 100         | ZDC: 100                                  |
| ADE: | -45.000000 | BDE:        | 0.000000    | CDE: 0.000000 <i>Fold Mirror</i>          |
| ADC: | 100        | BDC:        | 100         | CDC: 100                                  |
| IMG: | INFINITY   | 0.000000    |             | <i>Image Plane (CCD Camera)</i>           |



**TABLE II. CODE V specification data.**

**SPECIFICATION DATA**

|     |           |         |         |
|-----|-----------|---------|---------|
| EPD | 304.80000 |         |         |
| DIM | MM        |         |         |
| WL  | 656.27    | 632.80  | 525.02  |
| REF | 3         |         |         |
| WTW | 1         | 1       | 1       |
| XAN | 0.00000   | 0.00000 | 0.00000 |
| YAN | 0.00000   | 0.05717 | 0.08167 |
| VUX | 0.00000   | 0.00000 | 0.00000 |
| VLX | 0.00000   | 0.00000 | 0.00000 |
| VUY | 0.00000   | 0.00000 | 0.00000 |
| VLY | 0.00000   | 0.00000 | 0.00000 |

**APERTURE DATA/EDGE DEFINITIONS**

|         |           |         |           |
|---------|-----------|---------|-----------|
| CA      |           | CIR S6  | 12.500000 |
| CIR S5  | 12.500000 | CIR S8  | 12.500000 |
| CIR S7  | 12.500000 | CIR S10 | 12.500000 |
| CIR S9  | 12.500000 | CIR S12 | 12.500000 |
| CIR S11 | 12.500000 | CIR S15 | 20.000000 |
| CIR S13 | 12.500000 | CIR S17 | 20.000000 |
| CIR S16 | 20.000000 | CIR S19 | 12.500000 |
| CIR S18 | 12.500000 | CIR S21 | 15.000000 |
| CIR S20 | 15.000000 | CIR S24 | 15.750000 |
| CIR S22 | 15.000000 | CIR S26 | 15.750000 |
| CIR S25 | 15.750000 | CIR S34 | 40.000000 |
| CIR S33 | 40.000000 | CIR S37 | 45.000000 |
| CIR S35 | 40.000000 | CIR S41 | 37.000000 |
| CIR S39 | 55.000000 | CIR S45 | 45.000000 |
| CIR S43 | 55.000000 | CIR S48 | 40.000000 |
| CIR S47 | 40.000000 | CIR S50 | 10.160000 |
| CIR S49 | 40.000000 | CIR S52 | 10.160000 |
| CIR S51 | 10.160000 | CIR S54 | 9.000000  |
| CIR S53 | 9.000000  | CIR S57 | 13.250000 |
| CIR S55 | 9.000000  | CIR S59 | 13.250000 |
| CIR S58 | 13.250000 |         |           |

**TABLE II (cont). CODE V specification data.**

REFRACTIVE INDICES

| GLASS CODE  | 656.27   | 632.80   | 525.02   |
|-------------|----------|----------|----------|
| SSK4_SCHOTT | 1.614266 | 1.615305 | 1.621923 |
| SF8_SCHOTT  | 1.682505 | 1.684452 | 1.697362 |
| BAK4_SCHOTT | 1.565761 | 1.566704 | 1.572695 |
| F3_SCHOTT   | 1.608063 | 1.609545 | 1.619244 |
| BK7_SCHOTT  | 1.514323 | 1.515089 | 1.519867 |
| SF5_SCHOTT  | 1.666612 | 1.668457 | 1.680666 |
| SK11_SCHOTT | 1.561011 | 1.561883 | 1.567374 |

INFINITE CONJUGATES

EFL     -14063.1395  
 BFL     109.3923  
 FFL     -0.3236E+06  
 FNO     -46.1389  
 IMG DIS 108.0000  
 OAL     2301.9661  
 PARAXIAL IMAGE  
   HT     20.0458  
   ANG     0.0817  
 ENTRANCE PUPIL  
   DIA     304.8000  
   THI     650.0007  
 EXIT PUPIL  
   DIA     13.2190  
   THI     -500.5187

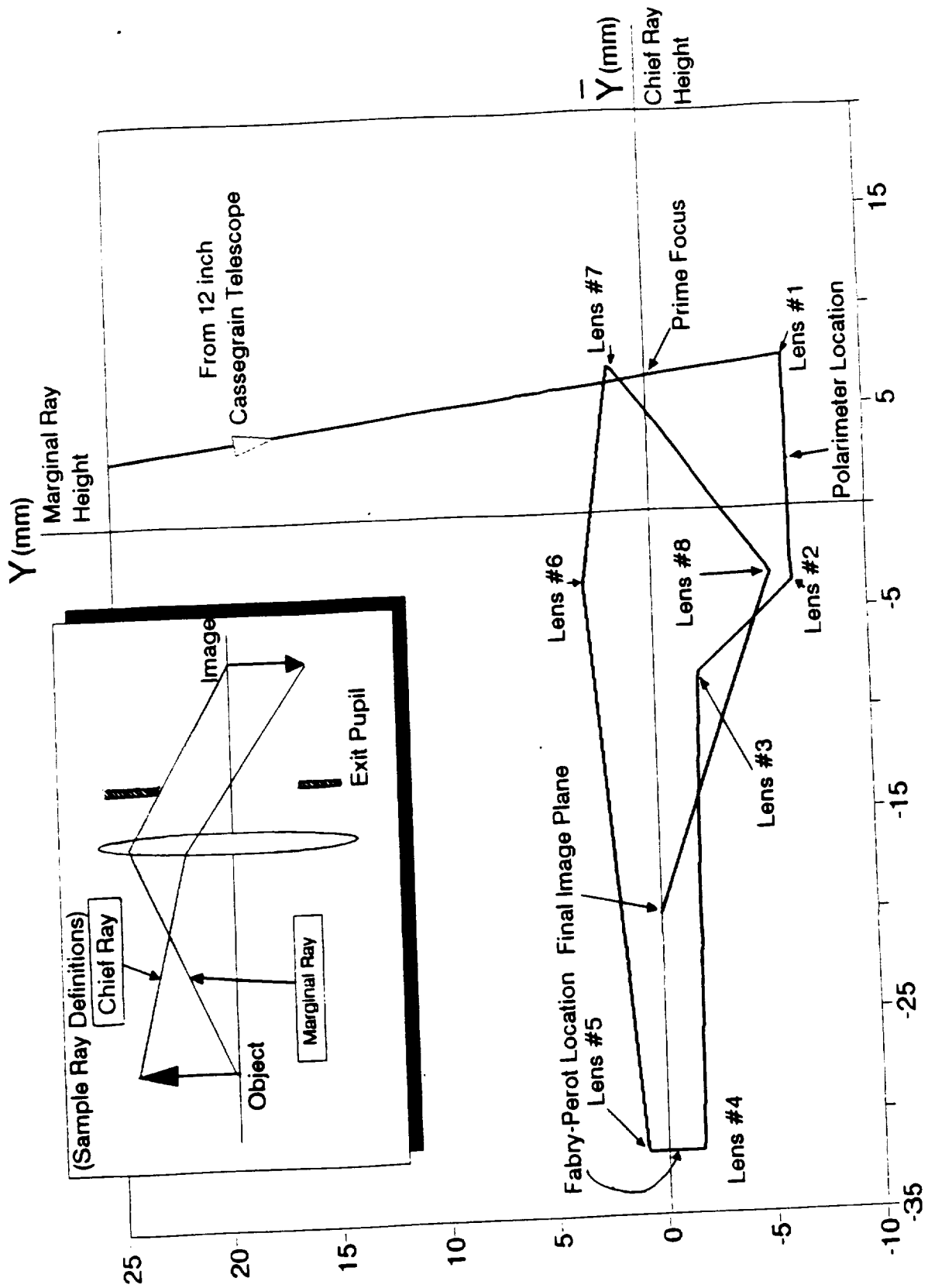


Figure 2 Y-Y diagram of the EXVM

On a  $y-\bar{y}$  diagram, horizontal lines represent collimated segments of the beam. Vertical lines represent telecentric beam segments. An image is formed where a line crosses the horizontal axis (i.e.  $y=0$ ). The value of  $\bar{y}$  at this point is the corresponding image height.

The distance between two points along a line on the  $y-\bar{y}$  diagram is found as follows: Find the area of the triangle formed by the origin and the two points of interest. The distance between the points equals twice this area divided by the optical invariant (0.217 mm/rad for the EXVM)

## (1.2) The Optical Invariant

The optical invariant is defined as

$$\mathcal{I} = y \bar{n}u - \bar{y} nu$$

where  $y$  and  $\bar{y}$  are marginal and chief ray heights, respectively. Similarly,  $nu$  and  $\bar{n}u$  are the marginal and chief ray angles (multiplied by the index of refraction of the medium). These values are as the basis of paraxial ray tracing.

The numerical value of the optical invariant can be measured, and will be the same, at any surface. Using the paraxial ray trace values at any surface of the EXVM (see Appendix A) yields a calculated optical invariant of  $\mathcal{I} = 0.2172$  mm/rad.

### **(1.3) Telescope**

The EXVM was designed around an existing 30 cm,  $f/15.5$ , Cassegrain telescope. A Cassegrain telescope was used because it is radially symmetric and has low angles of incidence. These criteria help minimize the instrumental polarization. Since it is placed before the polarimeter, it is important that the telescope affect the polarization of the incident light as little as possible.

### **(1.4) Relay Optics**

The light exiting the telescope is an  $f/15.5$  beam that is very nearly telecentric (chief ray angle = 0.004339 radians). The beam comes to focus about 25 cm beyond the back face-plate of the telescope. The CODE V specification places the polarimeter in the nearly telecentric beam between the telescope and the image. If the polarimeter is placed in this beam, the distance from the back of the telescope to the image will increase by 28 mm (computed using the CODE V model of the polarimeter). Therefore, whether or not the polarimeter is to be placed in this position must be considered during the alignment of the EXVM.

Lens #1 (MGLAO225) is placed one focal length (200 mm) beyond the image formed by the telescope. The light exiting lens #1 is, therefore, collimated. The

collimated area between lens #1 and lens #2 can be used for a Lyot birefringent spectral filter or as a position for the polarimeter. A maximum ray angle of 0.033548 radians ( $1.92^\circ$ ) occurs in the collimated beam for objects at the maximum field of view (4.9 arcmin of axis).

Lens #2 (MGLAO239) refocuses the beam in order to form an image for the correlation tracker. An  $f/23.4$  beam is produced.

The articulated fold mirror is controlled by the correlation tracker. Rapid computer-controlled adjustments of this mirror allow the effects of seeing fluctuations, wind, and instrument motion to be minimized. This is necessary in order to improve the resolution to 0.5 - 2.0 arcseconds for ground-based observations.

A beamsplitter (*not* shown in the original CODE V output) placed immediately after the articulated mirror provides the image for the correlation tracker. Options for beamsplitters are discussed in Section 1.7.

Lens #3 (SH325222) is the only negative lens in the EXVM. This lens nearly collimates the beam (marginal ray angle only -0.001344 radians). The blocking filters for the EXVM (whose center wavelengths depend on angle of incidence) are placed in this nearly collimated beam. The largest ray angles at the blocking filters are those coming from objects at the maximum field of view. The ray angles increase linearly from nearly zero (on axis) to 0.102462 radians ( $5.87^\circ$ ) for chief ray angles

corresponding to objects 4.9 arcmin off axis. Furthermore, as seen on the  $y-\bar{y}$  diagram (Fig. 2), this lens significantly shortens the overall system.

Lens #4 (SH322278) produces an  $f/73.2$ , telecentric beam. The Fabry-Perot interferometer is placed in this beam. The angles of incidence at the Fabry-Perot do not depend on field height (unlike a collimated beam). A maximum ray angle of 0.006831 radians is predicted by the paraxial ray trace. As shown in Fig. 1, this beam is so slow that nearly every surface of the Fabry-Perot will be in focus at the final image plane. These surfaces must, therefore, be kept very clean. The seal-unit of the Fabry-Perot should help in this regard, with only the outer windows requiring periodic cleaning.

Lens #5 (SH322279), as seen in the  $y-\bar{y}$  diagram (Fig. 2), acts as a field lens. A field lens decreases the height of the chief ray, thus allowing smaller clear apertures of the following elements.

Lens #6 (NCPAC064), refocuses the beam. An  $f/46.8$  beam is produced. If the lenses and mirrors following lens #6 are removed, an image nearly the same size as the final image (an  $f/46.1$  beam) is formed 290 mm after lens #6. This image would have the same orientation as the Cassegrain telescope image but would be inverted with respect to the final image.

Lens #7 (MGLAO059) further converges the beam. The  $f/11.2$  beam produces an image on a 15 degree, mirrored pyramid. This pyramid separates the beam into

four equally sized pieces. Each of these four beams will be focused onto its own CCD camera. The images will then be recombined by computer. The pyramid is placed in focus so that all of the light from a particular object point is reflected into the appropriate arm of the image dissector. If an expanded beam were incident on the pyramid, various rays from a given point object might be incident upon more than one face of the pyramid. Since it is in focus, the mirrored pyramid must be kept very clean.

Lens #8 (MGLAO123), refocuses the beam to produce the final image. There are four of these lenses; one in each of the arms of the image dissector. After a series of fold mirrors, the four final image components are formed on four CCD camera arrays.

### (1.5) Detectors

The final image is split into four quadrants. Each quadrant is imaged onto a separate detector. Four Thompson-CFS, TH 7896(A) CCD arrays are used as the detectors (Fig. 3). Each detector has  $1024 \times 1024$  pixels with a  $19 \times 19 \mu\text{m}$  pixel size. Half of each

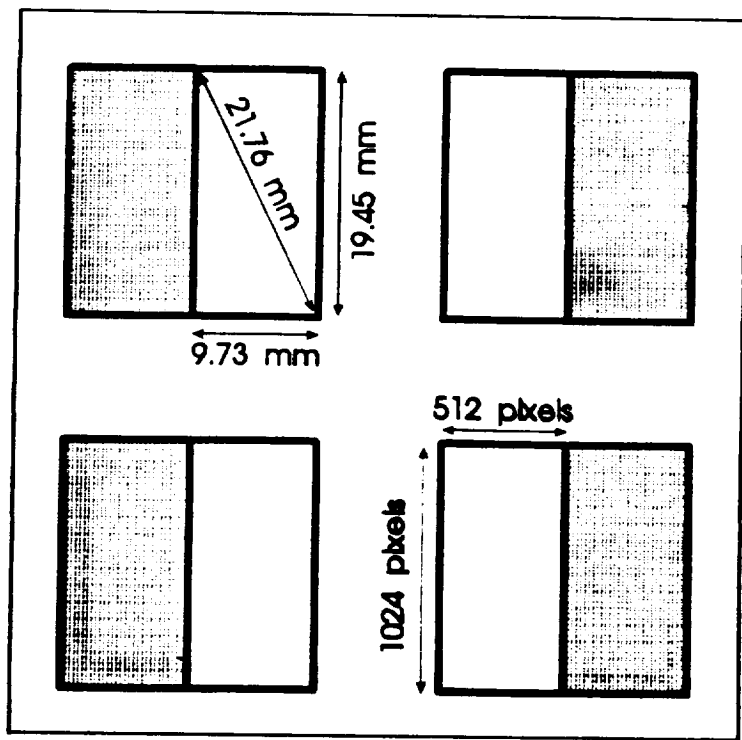


**Figure 3** Detector layout of the EXVM.



detector will be masked off for read-out purposes. Therefore, each detector's active area will be  $512 \times 1024$  pixels ( $9.73 \text{ mm} \times 19.45 \text{ mm}$ ). This corresponds to a center-to-corner distance of  $21.76 \text{ mm}$ . The combination of all four detectors yields a  $1024 \times 2048$  pixel array.

### **(1.6) Field of View and Image Sizes**

The original CODE V specification uses  $0.08167^\circ$  ( $4.9 \text{ arcmin}$ ) as its full-field object height. This height is the center-to-corner distance of a rectangular field of view having a 2:1 height-to-width ratio. Therefore, a  $4.38' \times 8.77'$  field of view was used as the CODE V specification data.

A rectangular aperture is to be placed at the image plane of the Cassegrain telescope. This aperture will act as a field stop. The size of this stop determines the field of view of the EXVM and the corresponding image sizes. The image sizes corresponding to various fields of view, calculated from the CODE V paraxial ray trace, are listed in Table 3.

TABLE 3. Fields of view and corresponding image sizes of the EXVM.

| Field of view (arcmin) | Cassegrain telescope image size (mm) | Correlation tracker image size (mm) | Final image size (mm) | Comments                        |
|------------------------|--------------------------------------|-------------------------------------|-----------------------|---------------------------------|
| 4.27×8.53              | 5.85×11.7                            | 8.87×17.7                           | 17.5×34.9             | Samex design goal               |
| 4.38×8.77              | 6.01×12.0                            | 9.10×18.2                           | 17.9×35.9             | CODE V design specification     |
| 4.76×9.51              | 6.58×13.0                            | 9.89×19.8                           | 19.5×38.9             | Completely fills four detectors |

\*equals the dimensions of the necessary field stop

The 4.8' × 9.5' field of view that completely covers the CCD arrays should not be used unless the image of the field stop on the CCDs is found to cause problems. This 4.8' × 9.5' field of view will have more vignetting and poorer image quality at the edge of the field than desired.

The paraxially calculated field of view for a single 19 × 19 μm pixel at the final image is 0.279 arcsec, regardless of the overall field of view used.

The image size at the detector for the correlation tracker plane is determined from the paraxial ray trace in Appendix A. A 4.38' × 8.77' field of view corresponds to a 9.10 × 18.22 mm image size at the correlation tracker.

### **(1.7) Beamsplitter Options**

A beamsplitter must be placed between lens #2 and lens #3 in order to provide an image for the correlation tracker detector. The original CODE V lens design does not include a model for this beamsplitter. During alignment of the EXVM, a 0.5 inch thick plate beamsampler was placed in the beam at  $45^\circ$ . This beamsplitter was flat to  $1/20$  wave (according to manufacturer's specification), and had an anti-reflective coating on its back surface. This beamsplitter caused unacceptable amounts of astigmatism. The separation between the sagittal and tangential foci was 21 mm at the final image. This separation was clearly visible by simply passing a card through the beam.

A pellicle beamsplitter used in this position would not introduce appreciable amounts of aberration to the system. However, the optics box for the EXVM will be subjected to vibrations from the clocked drive of the telescope, the articulated fold mirror, and the motors used in the polarimeter. Such vibrations tend to resonate the surface of a pellicle like a drum head. A pellicle cannot, therefore, be used.

CODE V was then used to model various beamsplitter types and configurations. Appendix B contains system drawings, RMS wavefront deviation values, wavefront aberration plots, and MTF curves for each of the options listed below.

Option #1 was the 1.57 cm thick plate inserted into the beam at  $45^\circ$ . The wavefront aberration plot clearly shows a full wave of astigmatism (at 633 nm) on axis.

Since this is a non-rotationally symmetric element, the on-axis astigmatism is not zero as might be expected. The astigmatism worsened off-axis, and coma (and other aberrations) became noticeable. The composite RMS wavefront error for the entire EXVM at best focus was 0.179 waves (at 633 nm).

Option #2 was inserting the 1.57 cm thick plate beamsampler into the beam at a smaller angle of incidence ( $15^\circ$ ). The on-axis astigmatism was nearly eliminated and off-axis astigmatism was reduced. The composite RMS wavefront error of the EXVM dropped to 0.058 waves. However, this option required the image to be reflected back toward the articulated fold mirror. This mirror will be mounted in a large gimbal system that will limit placement of the camera to be used. This option, therefore, would be very difficult to implement.

Option #3 uses a 2 mm thick plate beamsampler at  $45^\circ$  instead of the 1.57 cm thick plate. The EXVM's composite RMS wavefront error of this option is 0.064 waves. However, flatness is sacrificed by using such a thin plate. Melles Griot sells 2 mm thick plates flat to  $1/4$  wave.

Option #4 uses a 2.54 cm cube beamsplitter. The composite RMS wavefront error for the entire EXVM using this option is 0.012 waves; the lowest of all options considered. As seen in Appendix B, the on-axis performance for this option is diffraction limited. At full field, however, CODE V predicts sharp drops in the MTF curves. These drops, however, appear to be caused by vignetting that occurred in the

CODE V model as a result of not compensating for the increased optical path length caused by the cube beamsplitter. This vignetting problem is easily corrected during the alignment of the EXVM. The distance between lens #2 and lens #3 needs to be increased by 8.5 mm to accommodate the increased optical path length caused by the cube (see Section 2.1).

A cube beamsplitter is therefore recommended as a good choice for the correlation tracker beamsplitter. A cube should be chosen that only reflects a small portion (around 4%) of 525.0 nm light. The Melles Griot 03BSL145 non-polarizing (at 632.8 nm) beamsplitter already owned by the lab appears to work well, transmitting nearly all 525.0 nm light. Transmission/reflection characteristics were not provided at 525.0 nm, and should be obtained from Melles Griot.

## **(2) ALIGNMENT OF THE EXVM**

At the onset of the project, the optics-box intended to contain the post-telescope optics of the EXVM was still being designed. The lenses and fold-mirrors of the system were therefore assembled and aligned on a small optical bench in the laboratory. The elements were mounted 25 cm above the table, to match the height of a 30 cm Cassegrain telescope's optic axis when placed horizontally on another table. The entire

system was pointed out the door of the laboratory so that sunlight could be reflected off a 28 inch heliostat (sun tracking mirror) and into the EXVM for testing purposes.

## **(2.1) Relay Optics**

A 1 mW, 633 nm He-Ne laser was mounted such that its beam was parallel to the table at the desired height (25 cm). The mount for the laser allowed the beam's angle to be finely adjusted and the entire laser could be raised and lowered. The direct beam from the laser was used to define the optic axis during alignment.

The lenses and mirrors were mounted in suitable mounts and placed in their approximate positions on the optical table. The polarimeter, Cassegrain telescope, blocking filters, and Fabry-Perot etalon were not yet added to the system. Rulers and spacing-rods were used to get the spacing between lenses to within about  $\pm 5$  mm. Rolled-up lens tissues cut to the appropriate lengths make good spacer rods that minimize damage to the coated lens surfaces. The laser was directed down the center of the system. The reflections of the beam off of the lenses were used to remove any decentering or tilting present in the elements. This procedure is described below.

The only equipment needed is a small piece of white paper with a small hole in it. The hole should be only a few millimeters diameter (easily made with a sharpened pencil). The card is placed in front of the lens being aligned. The laser is allowed to

pass through the hole in the card and strike the lens. Since all of the lenses used in the EXVM are achromatic doublets, there are three separate reflections off of the lens (one from each surface). The beam should be blocked after the

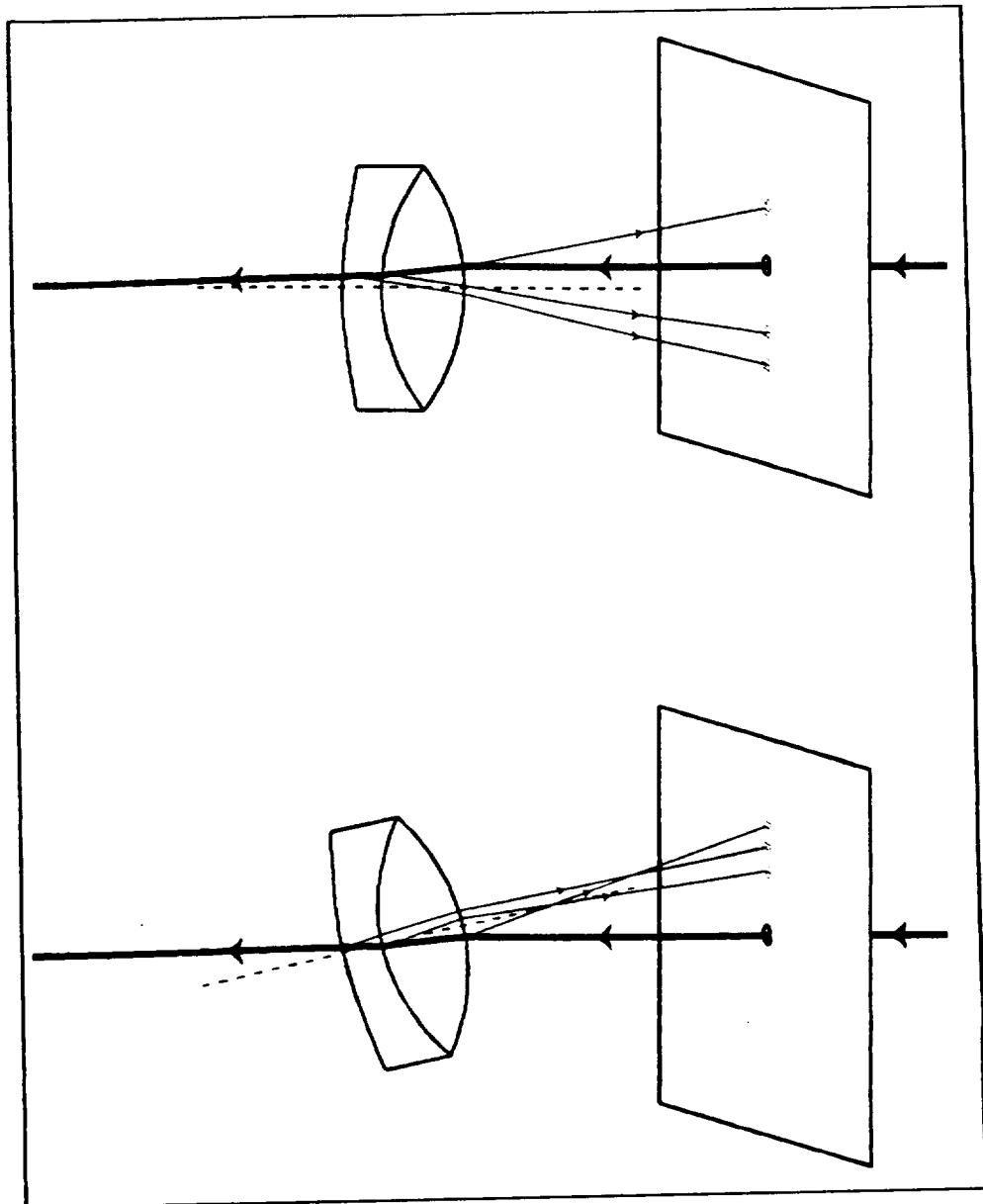


**Figure 4** A test for decentered and tilted lenses.

lens being aligned to avoid reflections off of subsequent elements. If the lens is perfectly aligned, all three reflections will travel back along the incident beam and through the hole in the card. If the lens is decentered or tilted, the reflections will not pass through the hole, but will instead strike the card in various places (Fig. 4).

By twisting the lens-mount, and translating it perpendicularly to the optic axis, the reflections off the lens can be made to pass directly back through the hole in the card. With a little practice and some trial-and-error, lenses can be aligned in this manner quite easily. Note that for low-power lenses, due to their less-curved surfaces, the card should be placed a considerable distance away from the lens to allow the reflected beams to fan out. Starting with the collimating lens (lens #1) and proceeding in order, all of the elements were aligned in this manner.

Once the lenses and fold mirrors were centered and untilted, the correct distances between the elements had to be achieved. These spacings could be measured with rulers and spacing-rods no more accurately than to within a few millimeters. Therefore, the behavior of expanded beams was observed and compared to the expected results given by CODE V. Figure 5 is a drawings of the predicted ray paths produced by on-axis and off-axis point sources placed at the back focal plane of the Cassegrain telescope.



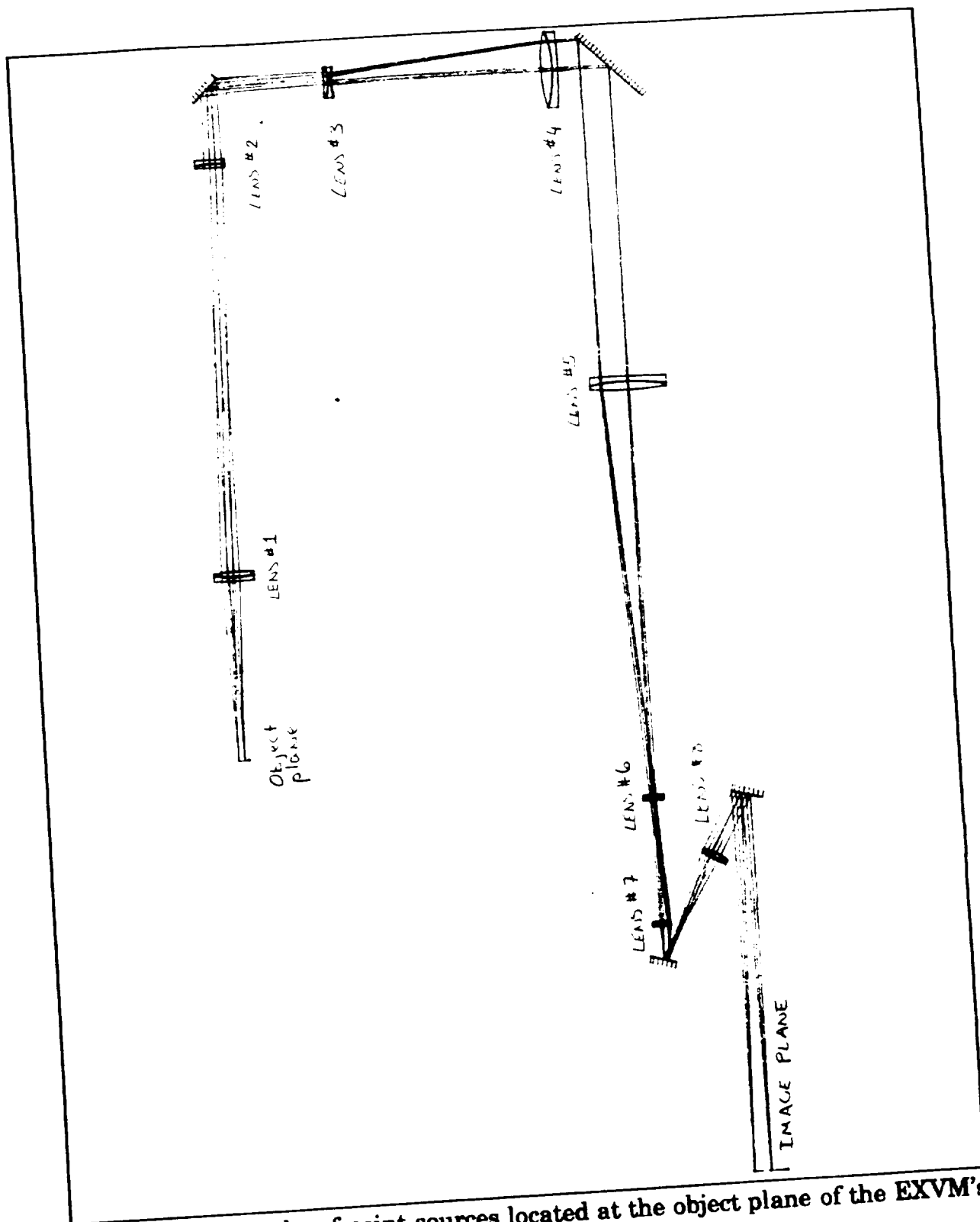


**Figure 5** Ray paths of point sources located at the object plane of the EXVM's relay optics.

A stop was needed to achieve the entrance and exit pupils that are produced once the telescope is added. Therefore, an adjustable aperture was set to 13 mm diameter and placed 225 mm after lens #1 (this pupil was determined by using marginal and chief ray information following lens #1, as given by the CODE V first-order ray trace of the entire system). A pinhole spatial filter added to the laser was used as a point object for the relay optics of the EXVM. The pinhole was placed 192 mm before lens #1.

The longitudinal (along the optic axis) position of the laser was adjusted until the light exiting lens #1 was collimated. A shearing plate interferometer (described in Section 2.2) was used to check for collimation. The angle of the beam was adjusted until the stop that was added between lens #1 and lens #2 was evenly illuminated. Finally, the transverse position (horizontal and vertical) of the pinhole was adjusted until the beam was centered in all of the lenses following lens #1. This procedure was iterated until all of these parameters were satisfied. At this position, the pinhole acts as point source in the center of the field of view (i.e. an on-axis point source).

The position of lens #3 was particularly difficult to get correct because the fold-mirror between lens #2 and lens #3 hindered measurement. Since the light exiting lens #3 is *not* collimated (although very close), a shearing plate interferometer could not be used. Instead, the position of the image formed after lens #4 was checked, and the beam between lens #4 and lens #5 was made to be telecentric. Note: be sure to add

the cube beamsplitter after lens #2 at this time. The thickness of the cube slightly affects subsequent image locations.

To determine if a beam is telecentric, an off-axis object is required. The laser and pinhole assembly was raised until the beam striking lens #4 was about 1 cm from the edge of the lens. The beam will strike lens #5 at the *same* height if the beam is telecentric. Slight adjustments to the positions of lens #3 and lens #4 gave the required image location and telecentricity.

The remaining lenses were adjusted in the same manner. Attaining correct image distances is a good way to ensure proper lens spacing. Once completed, the pinhole was removed from the laser, and any tilts or decenters caused by the alignment process were removed by observing beam reflections for an axial ray.

## **(2.2) Checking for Collimation with a Shearing Plate Interferometer**

Simply allowing a beam to reflect off a mirror, and comparing its size far away to its original size is *not* a recommended means of determining collimation. Particularly with a laser source, diffraction effects become so severe that the "size of the beam" is undeterminable far from the source. A shearing plate interferometer, however, provides a very accurate and simple way to verify collimation.

The shearing plate is a type of interferometer known as a lateral shearing interferometer. Malacara (1992) discusses many geometries of lateral shearing interferometers<sup>1</sup>, but the shearing plate is the simplest arrangement. A thin plate of glass (or other material) is inserted at 45 degrees into a collimated beam. As shown

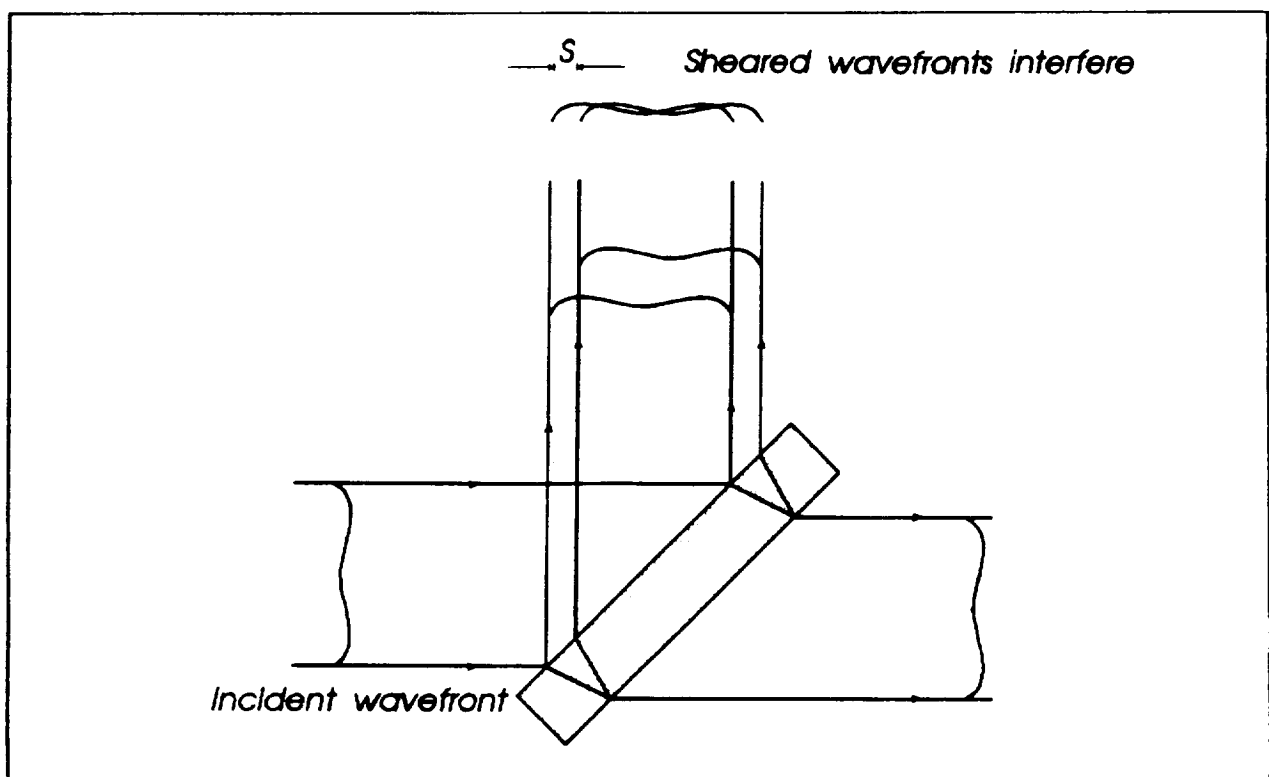


**Figure 6** Shearing plate interferometer.

in Fig. 6, the reflections of the beam off the front and back surfaces of the plate result in two wavefronts that have been laterally sheared a distance  $S$ . These two wavefronts interfere and the pattern they produce is observed and analyzed. Since the two beam paths are of unequal length, a coherent source (such as a laser) must be used.

For collimation testing, a slightly wedged plate is preferred. The plate is placed in the beam at a  $45^\circ$  angle. The wedge angle must be perpendicular to the  $45^\circ$  angle of rotation. For example, if the plate is rotated  $45^\circ$  horizontally, then the plate must be thicker at the top or bottom, creating a vertical wedge.

When the incident beam is perfectly collimated, the two interfering beams will both be plane waves. The resulting interferogram will be equally spaced, horizontal fringes (assuming a vertically wedged plate was used). If, however, the incident beam is not perfectly collimated, then the two interfering beams will be spherical waves (if the beam is unaberrated). The resulting fringe pattern is equally spaced linear fringes that are *not* horizontal. As a point source is moved through focus, the fringes rotate. Achieving horizontal fringes indicates collimated light.

A 2 mm thick, neutral density filter (thin-film type, O.D. = 0.04) was used as a shearing plate. The plate was placed after lens #1 at normal incidence. Numerous plates were tried, but this one was chosen because when the beam was reflected directly back at the lens, four straight, dark fringes with excellent contrast were present in the reflected interferogram. The plate was rotated *about the optic axis* until horizontal fringes were obtained. This ensured a vertical wedge angle.

The plate was then rotated  $45^\circ$  about its vertical axis. Figure 7 contains photographs of the interferograms created as the pinhole was moved along the optic

axis. This test was very sensitive. The pinhole was positioned to within  $\pm 1$  mm of its optimum spacing.

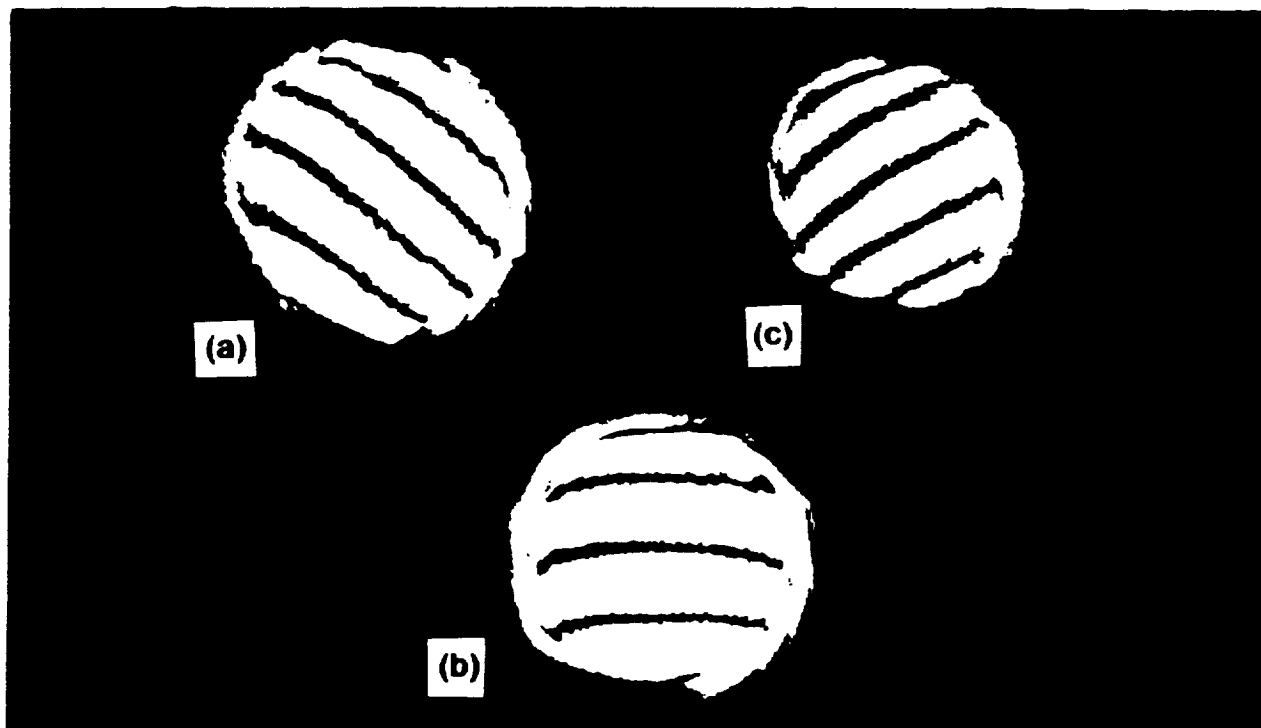


**Figure 7** Sequence of lateral shearing interferograms of the collimated area after lens #1 of the EXVM. A point source was passed through focus. (a) Outside the focus. (b) At the focus. (c) Inside focus.

### **(2.3) Adding the 20 cm Cassegrain Telescope**

Once the relay optics were acceptably aligned, the 30 cm Cassegrain telescope was added to the system. The back focal plane of the telescope was placed at the front

focal plane of lens #1. The procedure used to accurately align the telescope is outlined below.

The prefilter was placed on the entrance of the telescope. The prefilter reflects the He-Ne laser (633 nm) that was used for alignment. A pellicle beamsplitter was used, as shown in Fig. 8, to

reflect an on-axis point source (spatially filtered He-Ne laser) into the telescope. When the pinhole was positioned at the back

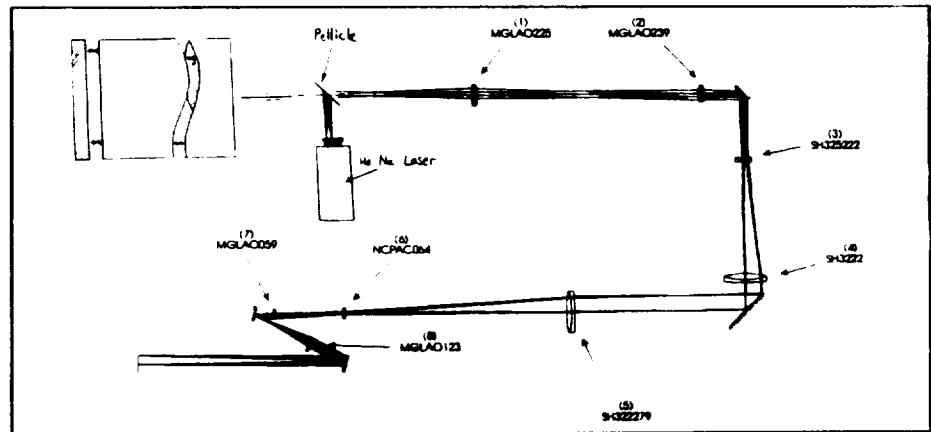


**Figure 8** The 12 inch Cassegrain telescope was aligned using a double pass configuration.

focal plane, collimated light exited the entrance of the telescope. This light then reflected off the prefilter, passed back through the telescope, through the beamsplitter, and into the EXVM's relay optics. The height of the telescope, its horizontal position, its angle with respect to the table, and its distance along the optic axis were all adjustable.

For the telescope to be perfectly positioned, three criteria had to be met: the light entering the rear of the telescope had to follow the exact same path as the light exiting the rear of the telescope, the light had to be collimated between lens #1 and lens #2, and the beam had to be centered in all of the lenses of the relay optics. A card with a

hole in it, held in the beam entering the telescope, allowed the returning beam to be seen. The returning beam passed through the hole and was the same size as the hole when the telescope was properly positioned.

A shearing plate placed after lens #1 was used to check for collimation. Figure 9 is the interferogram in collimated light. By moving through focus, the position yielding horizontal fringes was readily apparent. However, the fringes, although somewhat



**Figure 9** Photograph (and illustration) of a lateral shearing interferogram taken in the collimated area after lens #1. The non-linear fringes indicate wavefront aberration caused by the 12 inch Cassegrain telescope or its prefilter.

obscured by diffraction, were clearly *not* perfectly straight lines. This was the first indication we had that the telescope was causing some wavefront aberration (as discussed in Section 3.5).

Obtaining the precise alignment of the telescope was a tedious process. Iterative attempts finally yielded an acceptable alignment of the entire system. At this point, the image quality of the EXVM was ready to be tested.



### **(3) TESTING THE OPTICAL SYSTEM OF THE EXVM**

Once the components of the EXVM were assembled and aligned, the quality of the image produced was quantified. There are a number of different figures of merit frequently used to quantify image quality, such as the RMS wavefront error, the peak-to-valley wavefront error, a Zernike polynomial representation of the wavefront polynomial, the modulation transfer function (MTF), etc. Any or all of these values may be used to describe the quality of an optical system. Countless tests and procedures have been developed that allow these (and many other) parameters to be quantified.<sup>2,3</sup>

A number of tests were used to determine the imaging quality of the EXVM's optical system. A Foucault Knife Edge test was initially used, but the EXVM's aberrations were too small to be accurately measured with this test. A point-diffraction interferometer (Smartt Interferometer) was therefore used to obtain a contour-map of the systems wavefront and quantify the system's RMS and peak-to-valley wavefront error. A resolution test target was used to estimate the maximum spatial resolution the EXVM will be able to attain.

### **(3.1) Description of the Foucault Knife-Edge Test**

The Foucault Knife-Edge test is a simple test that allows aberrations in the exit pupil wavefront of a system to be observed. The results of a knife-edge test can be interpreted from mainly a geometrical optics point-of-view.

A point object placed in front of a perfect imaging system will produce a spherical wavefront leaving the exit pupil of the system. At each point along this wavefront, rays propagate perpendicularly to the sphere. These rays will all intersect at the center of curvature of the sphere. This point of intersection is the image of the point object.

A knife-edge oriented in a plane normal to the optic axis is passed through the beam exiting the system. If the image beam of the optical system is of sufficiently high f-number (i.e. the cone angle of the beam is sufficiently small) the entire cone of light will be able to enter the experimenter's eye. Looking into the beam allows the exit pupil of the system to be viewed directly. Alternately, a lens can be used to reimage the exit pupil onto a screen.

As illustrated in Figure 10, if the knife-edge is placed directly at the image point, the exit pupil will go from being evenly illuminated to being completely dark as soon as the knife edge reaches the image height. Light sources available in the lab are small, but they are not, however, true point sources. Subsequently, the "point images" produced actually have finite size. It is useful to consider an extended object as simply the

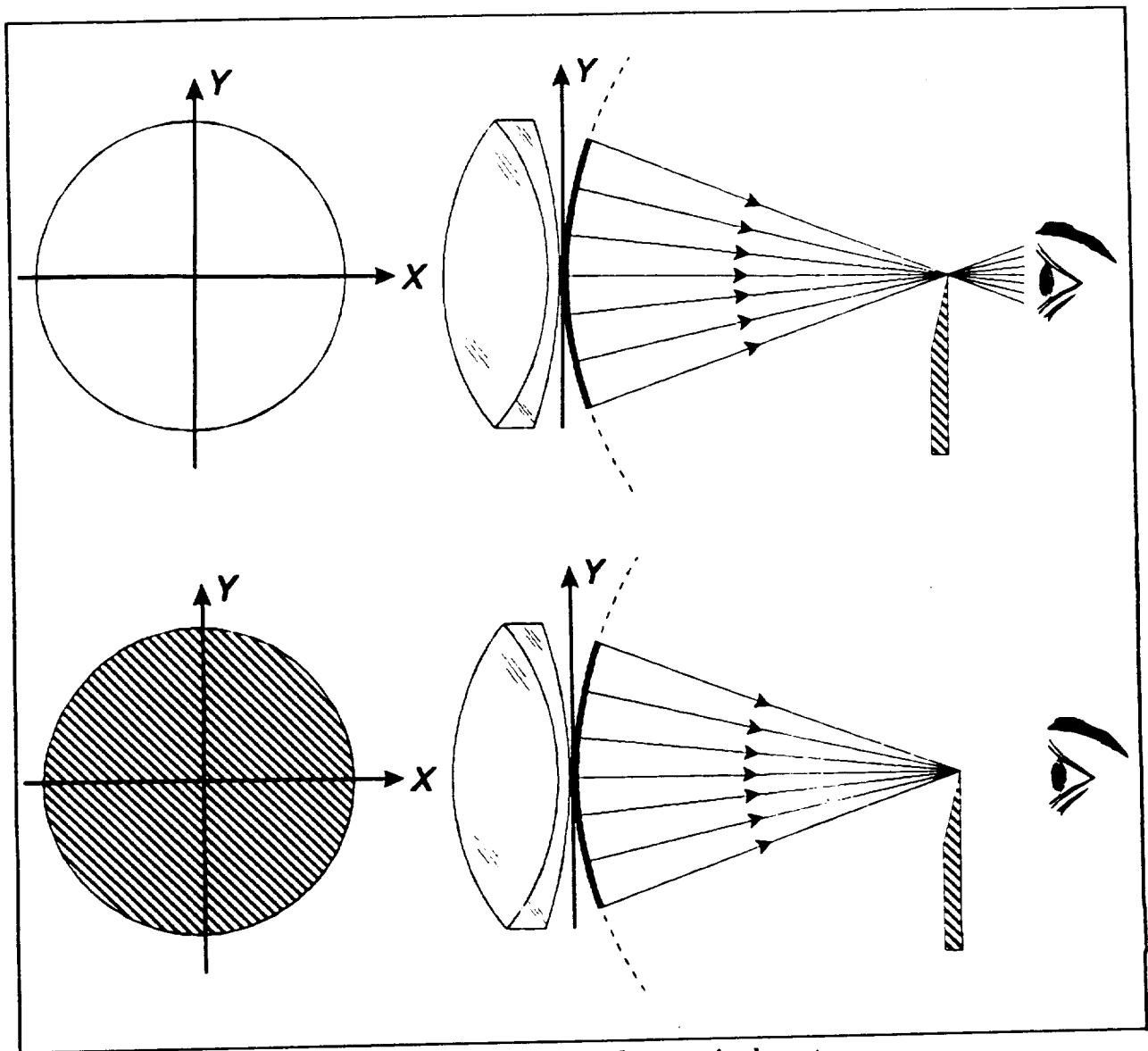


**Figure 10** Knife-edge test of an aberration-free optical system.

superposition of infinitely many point sources. Thus, as a knife-edge is passed through an extended image, the light from individual point sources of the object is extinguished. The resulting exit pupil will fade to darkness evenly as the blade is passed through the image. This uniform change in pupil intensity indicates perfect imaging when using the Foucault Knife-Edge Test.

Figures 11 and 12 describe the effect of passing a knife-edge through the beam when the blade is placed before or after the image position. As a blade is passed upward

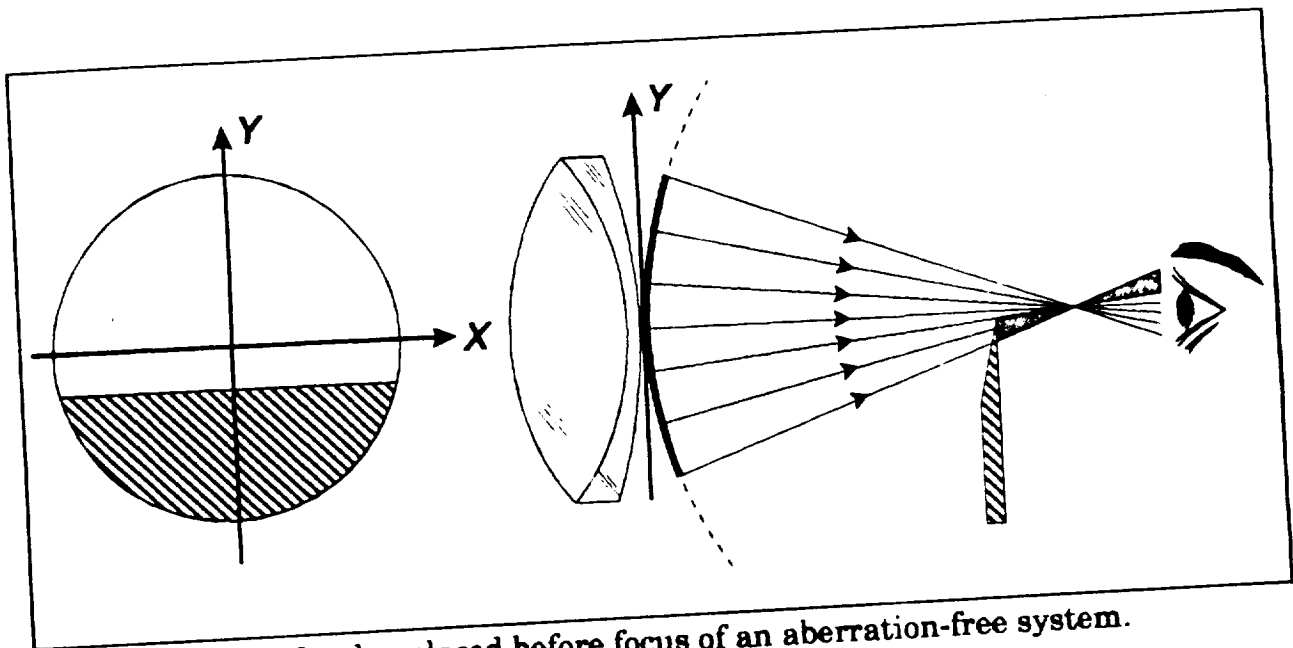


**Figure 11** A knife-edge placed before focus of an aberration-free system.

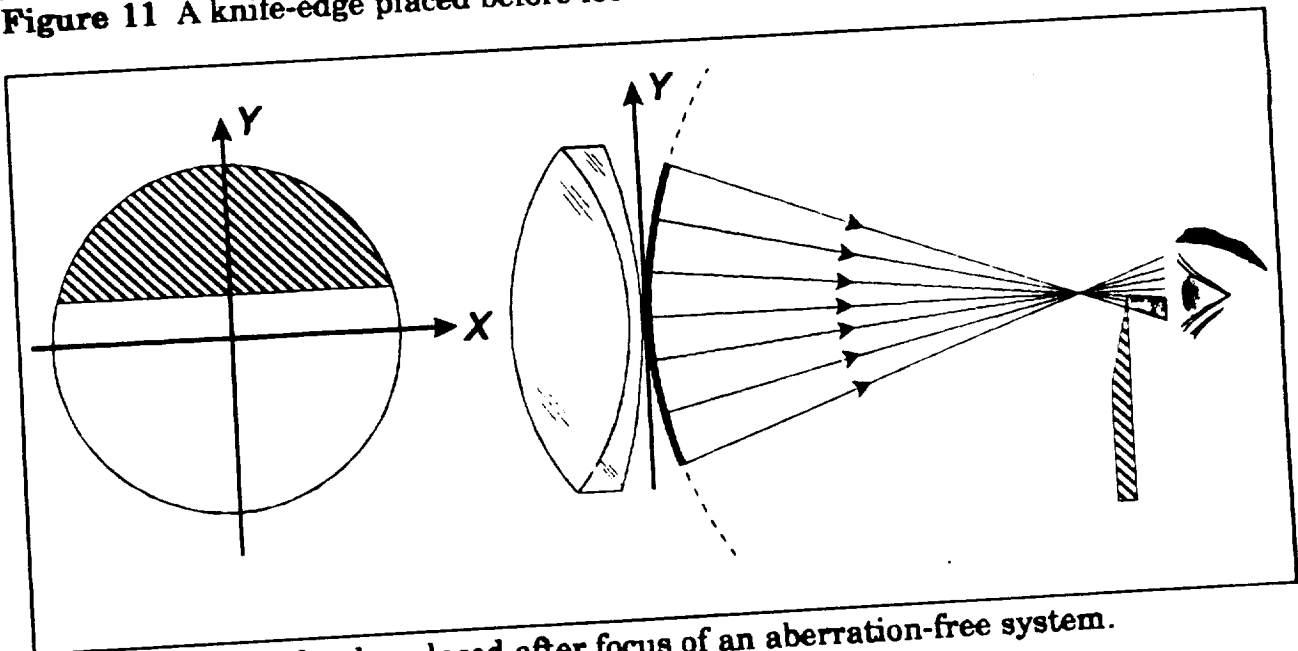


**Figure 12** A knife-edge placed after focus of an aberration-free system.

through a position between the exit pupil and the image, the rays from the bottom of the pupil are blocked first (Fig. 11). A straight shadow moves across the pupil from the bottom to the top. Similarly, if the blade is placed beyond the image plane, a straight shadow will pass from top to bottom across the exit pupil (Fig. 12) even though the blade was moved upward through the beam. It is important to note that for an aberration free system (i.e. spherical waves exiting), these shadows will be perfectly straight lines. Any curvature to the shadows indicates aberration, as will be discussed below. Finally, this test also provides a simple means of accurately finding the image position of an optical system.

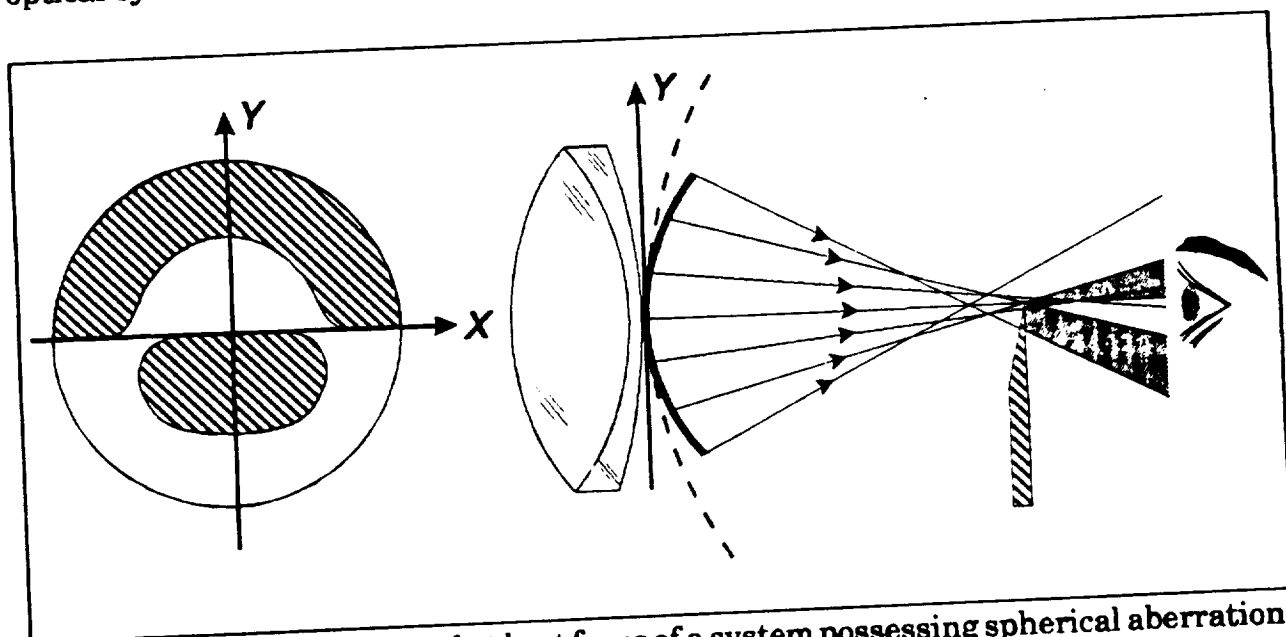


**Figure 13** Knife-edge placed at best focus of a system possessing spherical aberration.

Unfortunately, real optical systems rarely yield perfectly spherical exiting wavefronts when imaging point sources. Figure 13 illustrates a wavefront containing spherical aberration. As the knife-edge is passed through the beam in the position

indicated (best focal point) certain rays are blocked and certain rays are allowed to pass through. The exit pupil will not dim evenly as the blade is passed through the image. The shadow that passes across the pupil will not be a straight line.

The calculation of the knife-edge patterns for defocus, third-order spherical aberration, coma, and astigmatism are based on the transverse ray aberrations. The gradient of the wavefront aberration function is used to determine where each ray exiting the system intersects the image plane. If a ray is blocked by the knife-edge, then the pupil location from which that ray left will be dark. Rays that are not blocked result in illuminated pupil locations. These calculations and illustrations of the corresponding patterns can be found in Malacara.<sup>4</sup>

### **(3.2) Application of the Foucault Knife-Edge Test**

The post-telescope elements of the EXVM were tested with the knife-edge test. The telescope, polarimeter, blocking filters, and Fabry-Perot interferometer were not yet added to the system. The CODE V analysis of the optics indicated a nearly diffraction limited system. Any large aberrations discovered by the knife-edge test would be from misalignment of the optics, incorrect spacing between the elements, or having an element reversed.

A white-light pinhole source lamp was placed at the image plane of the Cassegrain telescope. An interference filter (540 nm center-wavelength) was inserted into the beam to both reduce the intensity of the beam and limit chromatic aberration effects when looking into the pupil. If a spatially filtered laser is used as the point source, the pupil of the system should be imaged onto a screen with a positive lens. (Do *not* look directly into the pupil due to the laser's high intensity.)

A razor blade mounted on a three-direction translational stage placed at the EXVM's final image plane was the testing apparatus. As the blade cut through the image, the exit pupil could easily be viewed by placing one's eye directly behind the blade and looking into the beam. Since this was an  $f/46$  beam, keeping one's eye nearly 10 cm behind the blade still allowed the entire cone of light to enter the eye. The exit pupil appeared to uniformly go from light to dark as the blade cut through the image. No discernable aberrations (like those mentioned in the previous section) could be observed. Any aberrations present due to the EXVM's relay optics were too small to be characterized by a Foucault Knife-Edge Test. This test was performed for both on-axis and off-axis sources.

The Foucault Knife-Edge test was only of limited use in analyzing the EXVM. Purposely introduced tilts of about  $5^\circ$  to various lenses were needed to introduce noticeable aberration to the pupil. However, such gross misalignments are easily removed

by checking beam reflections. More sensitive, interferometric testing was therefore needed.

### **(3.3) Description and Theory of the Smartt Interferometer**

To directly obtain the wavefront aberration caused by the EXVM, the exiting, nearly-spherical, aberrated wave-front is interfered with a spherical reference wavefront. The resulting fringe pattern is an optical path difference (OPD) contour-map of the aberration at the exit pupil. Many interferometric methods require two separate beams; one that passes through the system, and one to be used as the reference beam that does *not* pass through the system. These beams are then recombined to form the interferogram. The Mach-Zender and the Twyman-Green are examples of this class of interferometer. Such tests can be difficult to set up when testing large, complex systems, especially when limited space or facilities exist. Furthermore, any air turbulence, thermal fluctuations, or vibrations present cause considerable effects when the two separated beams are recombined.

The point-diffraction interferometer<sup>5</sup> (Smartt Interferometer) is a common path interferometer, meaning it has a configuration which divides light into a test beam and a reference beam *after* the light has passed through the optical system being tested. The effects of vibration, air currents, and thermal fluctuations are therefore considerably



reduced. The division of the beam is achieved by diffraction through a small pinhole. Scatterplate Interferometry<sup>6</sup> and Fresnel Zone Plate Interferometry<sup>7</sup> are examples of other common path interferometers using weak diffusers and zone plates, respectively, as the diffracting elements.

A Smartt interferometer is a polished glass or cleaved mica substrate on which an absorbing metal coating has been evaporated (usually gold or aluminum). The transmittance of the coating should be about 0.01. One or more pinholes are created in the coating either by vaporization with a focused laser or by shadowing with small spheres during evaporation.<sup>8</sup>

Figure 14 illustrates the operation of the Smartt interferometer. The interferometer is placed at the image point of the wavefront to be tested. The point-spread function of the system is imaged

onto the device. A pinhole with a diameter less than the size of the point-spread function will diffract a portion of the incident light into a spherical wave. This spherical wave acts as a reference wave and is interfered

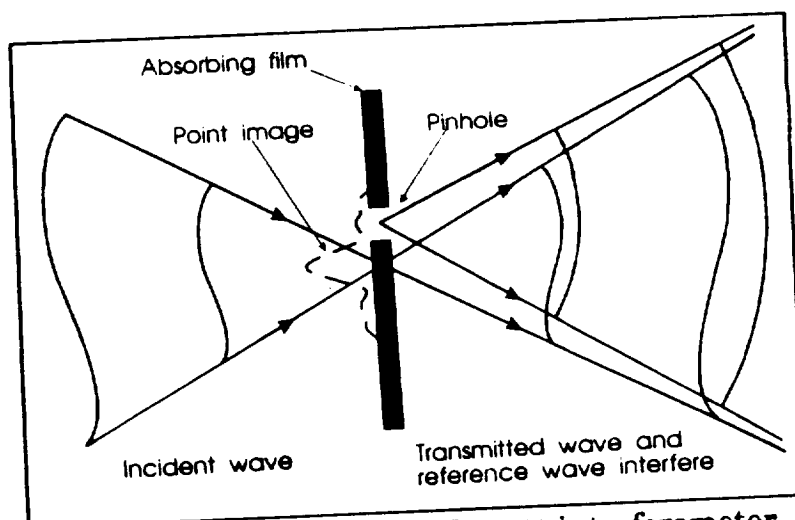


**Figure 14** Principle of the Smartt interferometer.

with the test wave that passed, attenuated, through the absorbing film of the

interferometer. The film's transmittance or the pin-hole diameter may be changed to equalize the test and reference waves' intensities, hence maximizing fringe visibility. An estimation for the proper pin-hole radius for an aberration-free system is given by<sup>9</sup>

$$a \sim \frac{0.1 \lambda}{NA}$$

where  $\lambda$  is the wavelength being used and  $NA$  is the numerical aperture (sine of the marginal ray angle) of the exiting beam.

Due to its portability and simplicity, the Smartt interferometer is well suited for the interferometric testing of single optical elements, telescopes, and even complex multi-element systems. All that is required is an accessible point image produced by the system from a point object at the desired conjugate. Since this is an equal-path interferometer, temporal coherence of the source is not required. Smartt reports successful telescope tests have been performed using a second, first, or zero magnitude star near the zenith (where seeing is the best) as the point object. Smartt was also able to use a 2 md He-Ne laser at a distance of 2.4 km with only  $\sim 0.04 \lambda$  error due to the non-infinite conjugate.<sup>10</sup> Excellent fringes were also obtained of a 20 cm Schmidt-Cassegrain telescope<sup>11</sup> indoors with a laser source distance of about 30 m.

### (3.4) Application of the Smartt Interferometer

Dr. Raymond Smartt (National Solar Observatory, Sunspot, NM, 88349) provided a Smartt interferometer for this project. The device had numerous pinholes scattered across it, ranging from 12 to 27 micrometers in diameter.

The 30 cm Cassegrain telescope was tested and aligned using the Smartt interferometer. Due to laboratory constraints, placing a laser source at a nearly-infinite conjugate was not

feasible. Instead, a double-pass configuration was used as illustrated in Fig. 15. A 1 m $\mu$ , 633 nm, He-Ne laser with a pinhole spatial

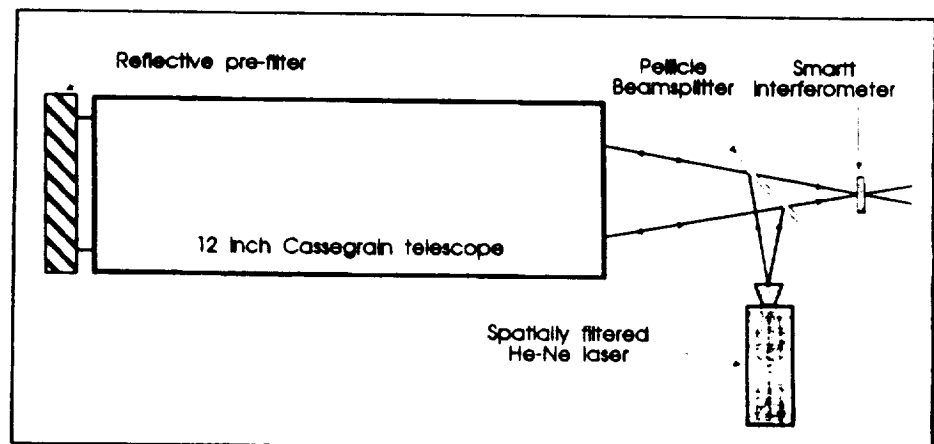


**Figure 15** The telescope was interferometrically tested in double-pass.

filter was used as a source. The source was reflected off of a 2 inch diameter pellicle beam sampler and into the telescope. The beam exiting the front of the telescope was reflected off of the reflective pre-filter back into the telescope. The pre-filter is a 30 cm diameter, 2.0" thick fused-silica window with a 525 nm interference filter coating (60% transmission, 60 nm bandpass) on its inner (i.e. toward the telescope) surface. This

coating reflects >97% at 633 nm (He-Ne laser), making it an excellent mirror for this test. At the time of purchase (1988), the pre-filter's flatness was better than 1/4 waves over its entire aperture. The present (1993) condition of the pre-filter is unknown. The beam then passed back through the telescope, through the beamsplitter, and formed a point image at the telescope's focal point.

To ensure that the proper conjugates were used, it was important that the source be located exactly at the telescope's back focal plane. Hence, collimated light reflects off the pre-filter and the resulting image is also at the back focal plane. A shearing-plate was not sensitive enough to ensure collimated light exiting the telescope; a few centimeters range of object positions appeared to result in collimated light. A more sensitive test proved simply to be a hole punched in a white card that allowed only a select cone of rays to enter the telescope. When the returning rays followed the exact same path as the entering rays (i.e. they returned perfectly through the hole in the card from which they came) the system was aligned. The post-telescope optics of the EXVM were then positioned beyond the Cassegrain image at the appropriate location. Proper on-axis alignment was easily obtained by checking for collimated light after lens #1 (using a shearing-plate) and verifying that the beam was centered in both telecentric lenses (#4 and #5).

The interferometer was mounted on a translational stage that allowed motion along, and transverse to, the optical axis. Translation along the optical axis allows the

point of best focus to be found (i.e. the fewest fringes across the pupil). Tilt can be introduced to the interferograms by displacing the pinhole transversely, away from the center of the point spread function. However, fringe visibility changes dramatically as the pinhole moves across the point spread function because the intensity ratio of the test and reference beams changes.

The Smartt interferometer was placed at the telescope image (before lens #1). The collimating lens (lens #1) provided an image of the telescope's entrance pupil, allowing the interferometric fringe pattern to be observed without being obscured by diffraction effects (a second positive lens was inserted to decrease the image size to that of a CCD camera array). The inefficiency of the beamsplitter (about 4% reflection) resulted in an image with low irradiance. In a darkened laboratory, the fringe pattern was visible, but very small. Enlarging the image resulted in decreased brightness. A CCD camera placed at the image allowed the fringe pattern to be easily viewed on a television set, enlarged and with improved contrast. A digital frame-grabber was used to store the CCD images for later analysis (see next section). Interferograms were recorded for on-axis and off-axis sources.

Next, the relay optics of the EXVM were tested. The spatially filtered laser was placed on-axis at the telescope image location. Proper positioning was ensured by testing for collimation after lens #1 using a shearing plate. All of the relay optics (including the image dissector and correlation tracker beamsplitter) were included in this test.

Interferograms were made at the final image position for on-axis and off-axis (in both the  $x$  and  $y$  directions) objects. Object height was easily monitored observing the position of the telecentric beam in lenses #4 and #5. The intensity of the interferograms was very high, and they were very stable. The fringes were traced by hand directly onto paper, saving time and computer disc space.

Finally, the relay optics and telescope were tested together. The interferometer was placed at the final image position of the EXVM. The laser source reflected off the pellicle beam-sampler, passed through the telescope, reflected off the pre-filter, passed back through the telescope, went through all of the relay optics of the EXVM, and finally through the Smartt interferometer and onto a CCD camera. Since in this configuration the telescope was tested in double-pass and the relay optics were tested in single-pass, the resulting interferograms are of limited value for system analysis.

However, this configuration *does* demonstrate the versatility of the Smartt interferometer. Despite the long optical path (about 10 m) the fringe pattern was surprisingly stable. The pattern *did* appear to slowly "churn" due to thermal fluctuations along the beam's path, and bumping the table did cause the fringes to vibrate (but not disappear). Overall, this test was surprisingly insensitive to a less-than-ideal laboratory environment, making the Smartt interferometer an extremely useful tool for both laboratory and in-the-field system characterization.

### **(3.5) Analysis of Interferograms of the 30 cm Cassegrain Telescope**

The interferograms produced by a Smartt interferometer represent contour maps of the wave-aberration of the optical system being tested (unlike some shearing-interferometers that represent the gradient of the wave-aberration and require computer reduction of all but the simplest data). Every fringe indicates one wavelength of phase aberration.

However, the telescope of the EXVM was tested in a double-pass configuration. Provided the aberrations are relatively small, each ray will pass back along its original path.<sup>12</sup> The effects of any defects in the elements of the telescope will, therefore, be doubled. When analyzing the interferograms taken of the 30 cm Cassegrain telescope, it is important to realize that each fringe represents only 1/2 wave of aberration, due to this double-pass configuration.

When analyzing interference fringes, it is generally desirable to use linear fringes instead of the circular central fringes for the following reasons:<sup>13</sup>

- 1) The linear pattern is easily recognized by x-y scanning devices.
- 2) Ambiguities in fringe-order, which are possible with circular fringes, are avoided.
- 3) A reasonably uniform light flux density is achievable over the entire aperture.
- 4) The pupil is sampled more completely for curve-fitting procedures.

Linear fringes are created by introducing tilt between the interfering wavefronts. Tilt is achieved in the Smartt interferometer by simply offsetting the pinhole from the center of the point diffraction pattern. Any deviation of the fringes from equally-spaced, straight parallel lines represents wavefront aberration. Interferograms of the primary aberrations (Spherical Aberration, Coma, and Astigmatism) are discussed and illustrated by Kingslake<sup>14</sup> and more recently by Malacara.<sup>15</sup> Malacara's book proves to be an indispensable guide in the analysis of interferograms.

However, when significant tilt is added with the Smartt interferometer, the fringe visibility is dramatically influenced. Carefully scanning the interferometer's pinhole across the point diffraction pattern revealed only a few positions that gave reasonable fringe visibility. Numerous pinhole sizes were used in order to find the best fringe visibility. Choosing larger pinholes for tilted (off-centered) interferograms seemed to help. Figure 16 is a set of on-axis interferograms of the EXVM's Cassegrain telescope with tilts introduced in various directions. (The off-axis interferograms were identical to the on-axis results. All analysis conducted below is therefore valid for all object heights being considered.) The central fringe offers an easily understood contour map of the wave-aberration. While the tilted fringes are simply the same contour map on an incline, they are less intuitively interpreted.

The top set of near-linear fringes was chosen for analysis. This set was chosen for two reasons: the eleven dark fringes across the pupil allow accurate sampling of the





**Figure 16** On-axis interferograms of the 12 inch Cassegrain telescope taken in double-pass. Each fringe represents two waves of aberration.

fringe-order across the entire wavefront, and the fringe contrast is fairly good across the entire pupil. Figure 17 illustrates how the fringe pattern was sampled. The fringes of the interferogram were directly traced onto another sheet of paper using a light-table. Alternately, a sheet of transparency could have been used. A  $32 \times 29$  grid was overlaid onto the traced fringes. Note that the pupil is not perfectly round. This distortion was

caused by the disparities between pixel dimensions of the CCD camera, television monitors, and thermal wax printer used to obtain a hardcopy of the fringe pattern.

Numerical values were assigned to each element of the superimposed grid. A value of zero was chosen for the bottom light fringe. The first dark fringe was assigned a value of five. The next light fringe was 10, the next dark fringe 15, etc. When a grid element contained the boundary between dark and light fringes, an intermediate value was chosen in accordance with the ratio of dark-to-light within the element. The resulting grid was entered as a  $32 \times 29$  array into IDL, a plotting/graphics program run on the laboratory's Digital MicroVAX II. Since the telescope was tested in double-pass, one fringe in the interferogram corresponds to only half-a-wavelength of aberration. Using the numbering scheme described above, 20 units is equivalent to one wavelength of aberration at 633 nm.

A subroutine was written that allowed a linearly varying tilt term to be added to every element of the array. Positive or negative tilts could be added to the array in either the x or y-direction. The subroutine also calculated the peak-to-valley wavefront aberration (the maximum array value minus the minimum array value) and the RMS wavefront aberration (the root-mean-square difference between each element and the average value across the pupil). Tilts were added until the RMS wavefront aberration was minimized.

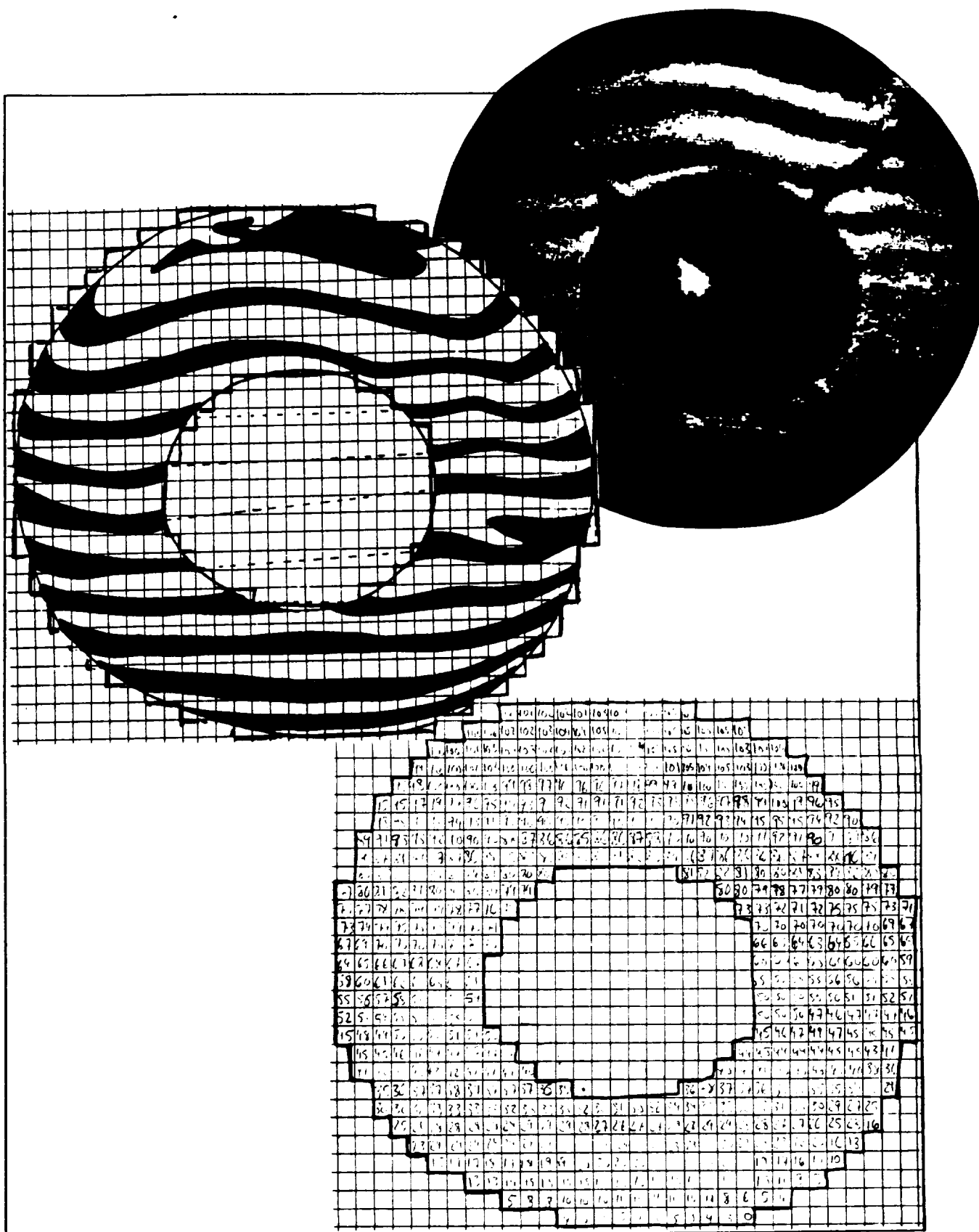


**Figure 17** Method for sampling the telescope interferograms.

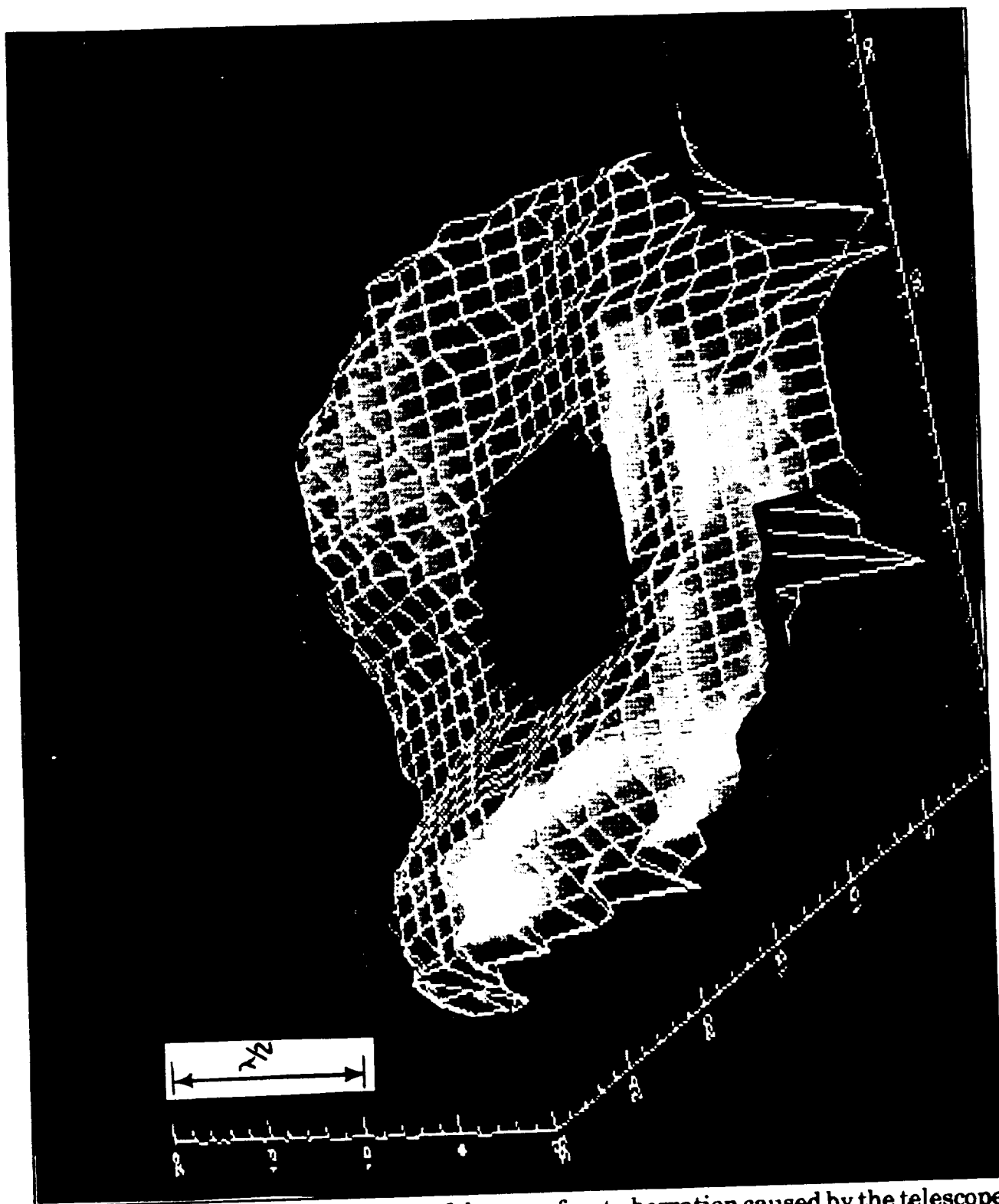


**Figure 18** Surface representation of the wavefront aberration caused by the telescope and/or prefilter.

Figure 18 is a three-dimension surface created by IDL representing the shape of the wavefront aberration, tilted to achieve minimum RMS deviation. Although this surface was created by tilting the top interferogram of Fig 16, it is clearly seen that the central interferogram of Fig. 16 is simply a slightly tilted contour map of this surface. The peak-to-valley wavefront aberration of the telescope is 0.85 waves at 633 nm (1.02 waves at 525 nm). The RMS wavefront aberration is 0.17 waves at 633 nm (0.20 waves at 525 nm).

The main characteristics of this aberration are the two vertically elongated humps on either side of the central obscuration, and a roll-off around the outer edge of the pupil. The telescope was tested in a horizontal position. Deformation of the primary mirror, secondary mirror, or the prefilter caused by lying on their sides could be the cause of the elongated humps. The edge of one or more of the elements may have been rounded off during polishing; possibly causing the observed roll-off. Alternately, a slight misalignment of the elements of the telescope may have caused a non-rotationally symmetric aberration.

Regardless of the origin of the telescope's aberration, the 0.20 waves RMS of aberration (at 525 nm) should not significantly affect the EXVM's performance. The maximum wavefront deviation is about 0.5 waves. Appendix A of Williams & Becklund's book<sup>18</sup> shows the calculated MTF curves due to various amounts of primary aberrations. From these curves, it appears that 0.5 waves of any aberration has little effect on the

maximum resolvable frequency. The 12" Cassegrain telescope should be able to achieve the desired 0.5 arcsecond resolution.

### (3.6) Analysis of Interferograms of the Relay Optics

The on-axis interferograms of the relay optics are shown in Fig. 19. The center interferogram is almost free of fringes and the tilted interferograms are nearly straight, parallel lines. These fringes indicate excellent imaging with nearly diffraction limited performance on-axis.

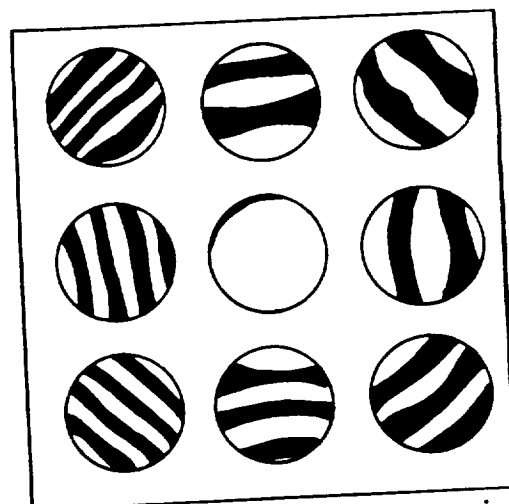
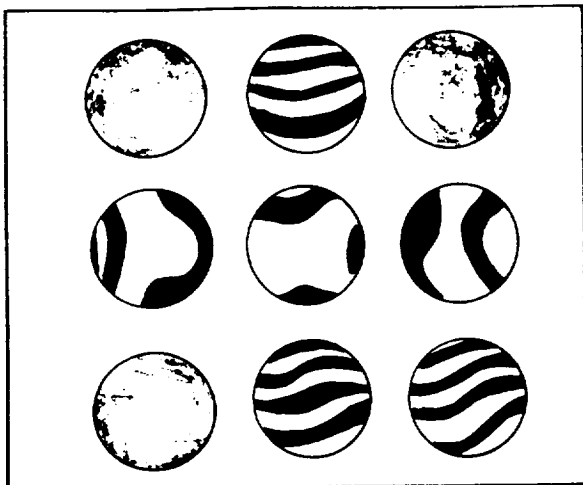


**Figure 19** On-axis interferograms of the relay optics tested in single-pass.

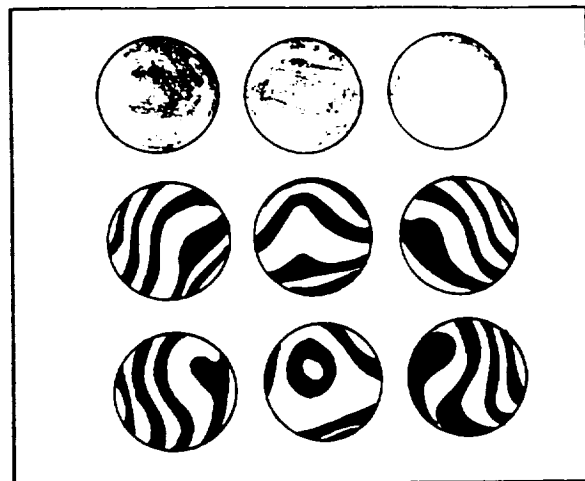
Figure 20 contains interferograms obtained with an object at the top of the field of view.

Figure 21 represents the bottom of the field. Interferograms from the left and right extremes appeared symmetric, and the leftmost (positive x-direction) interferograms are shown in Fig. 22.

The relay optics (including the cube beamsplitter) should have been rotationally symmetric. The interferograms indicate an asymmetry between the top and bottom full fields of view. Such an asymmetry might be caused by a slight misalignment or an imperfect element in the system.



**Figure 20** Top of the field-of-view of the relay optics. Shaded images indicate insufficient fringe contrast.



**Figure 21** Bottom of the field-of-view.

Each off-axis interferogram displays small amounts of both astigmatism and coma. The bottom field is the worst, with about one wave of coma (and a small defocusing) being the dominant aberration. Figure 23 is the theoretical MTF caused by one wave of coma.<sup>17</sup> A slight decrease in spatial resolution is predicted for objects at the full field of view.

The MTF curves of the telescope and of the relay optics cannot be simply combined to find the overall MTF of the EXVM. The wavefront aberrations of the two subsystem could be combined,

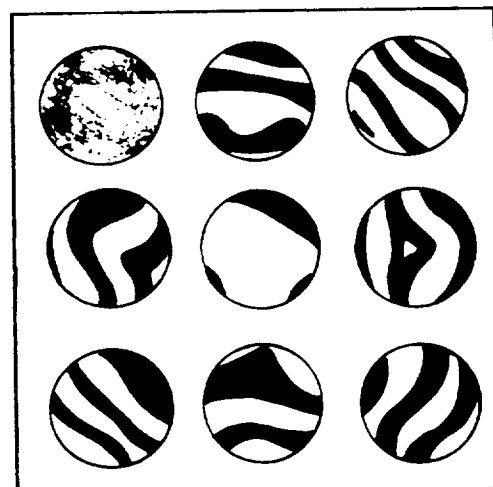


**Figure 22** Leftmost field-of-view.

but this was not deemed necessary. Due to the quality of each subsystem, the CODE V

MTF curves for the EXVM in Appendix A should be fairly representative of the actual system performance.

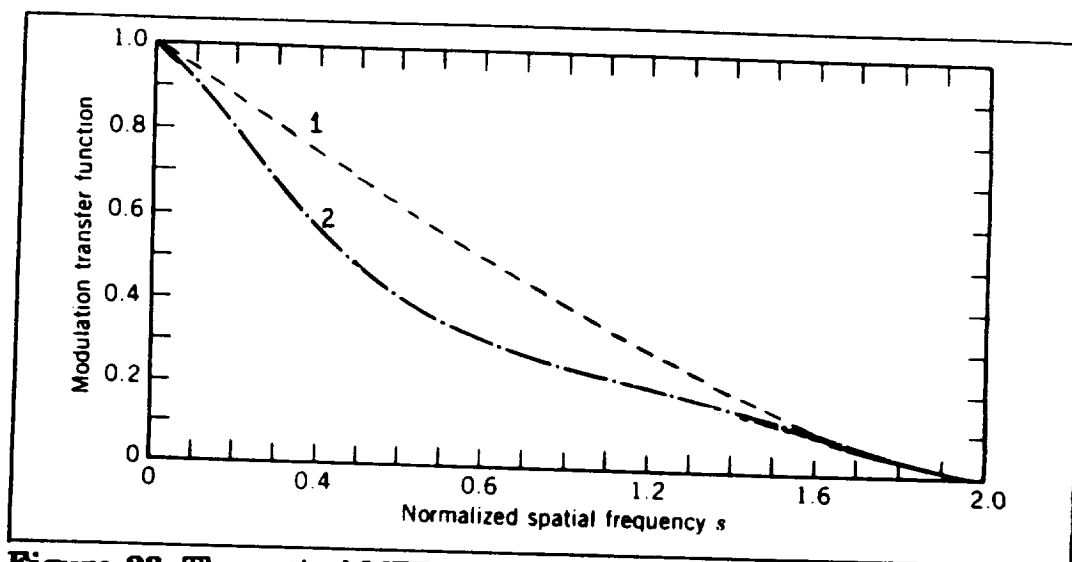


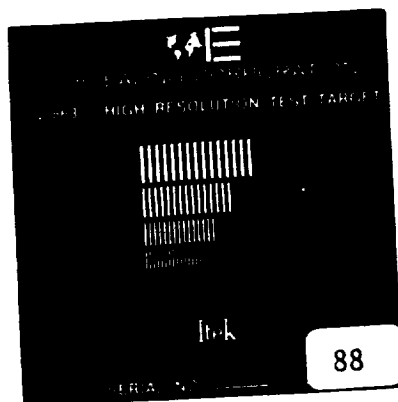
**Figure 23** Theoretical MTF curves for (1) a diffraction limited system, (2) a system with one wave of third-order coma at paraxial focus.

### **(3.7) Application of the Resolution Test Target**

A resolution test target (Fig. 24) was used as an object for the EXVM's relay optics. A high intensity white-light source (with a ground glass screen) illuminated the target from behind. At the proper object location, the light after lens #1 is collimated. A shearing plate interferometer could *not* be used to test for collimation due to the inherent lack of temporal coherence of a white-light source. Proper object position was obtained simply by achieving correct intermediate and final image locations.

A CCD camera was placed at the image plane. The image of the test target was viewed, greatly magnified, on a television. The maximum resolution (i.e. minimum line





| Group 1 | Group 2 | Group 3 |
|---------|---------|---------|
| 1.00    | 10.00   | 100.0   |
| 1.26    | 12.59   | 125.9   |
| 1.58    | 15.85   | 158.5   |
| 2.00    | 19.96   | 199.6   |
| 2.51    | 25.12   | 251.2   |
| 3.16    | 31.63   | 316.3   |
| 3.98    | 39.82   | 398.2   |
| 5.01    | 50.14   | 501.4   |
| 6.31    | 63.13   | 631.3   |
| 7.95    | 79.48   | 794.8   |
| 10.00   | 100.00  | 1000.0  |

**Figure 24** The resolution target (actual size) and corresponding line-pairs/mm used to test the EXVM.

pairs per millimeter) for on-axis and off-axis object positions was measured by determining the finest line pairs resolvable on the television. In all cases, the resolution of both vertical lines and horizontal lines was measured. This was done merely by measuring the test target both at 0° and rotated by 90° at each object position.

Attempts were made to measure the resolution of the relay optics with the Fabry-Pérot and the blocking filters added to the system. These filters allowed only a fraction of the light through. A bright enough source was not available to provide adequate illumination at the CCD array. The Fabry-Pérot and the blocking filters should not, however, significantly degrade the system quality.

### (3.8) Resolution Test Target Analysis

Figure 25 is an image of the resolution test target that has been digitized from the CCD camera. Due to the printing process involved, this figure does not adequately show the resolution that could be obtained simply by looking at the television screen. With the test target on-axis, 79.48 lines/mm was the smallest

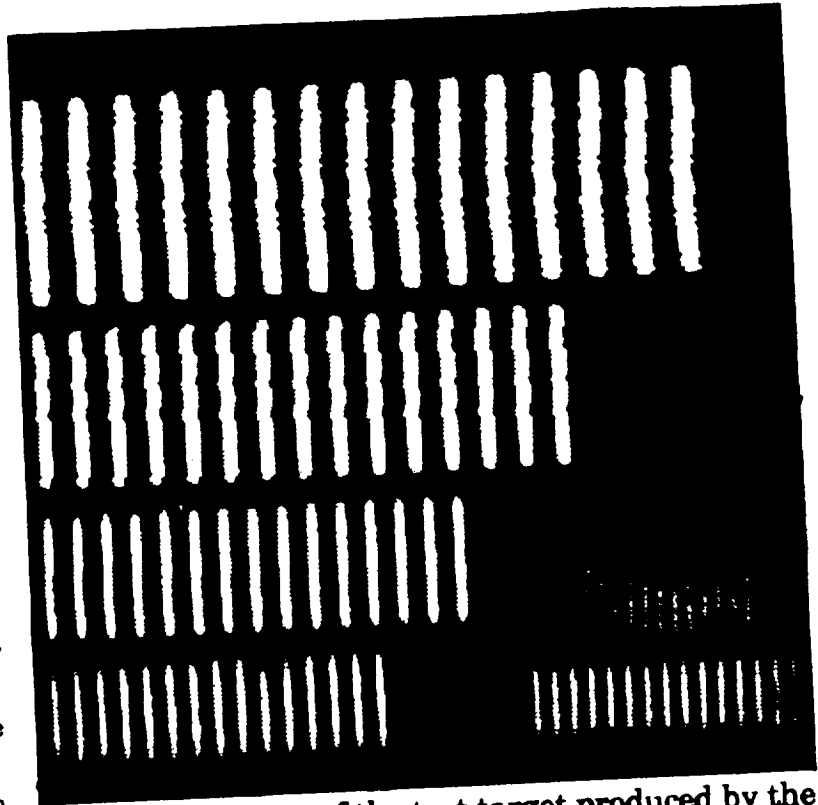


**Figure 25** Image of the test target produced by the relay optics. The second bar-set is show here.

resolvable target segment. When the test target was placed at full-field (top, bottom, left, or right), 63.13 lines/mm was resolvable. The system resolution was the same for both vertical lines and horizontal lines on the test target.

The paraxial ray trace of Appendix A is used to relate the spatial resolution at the telescope's image plane to the angular resolution that should be attainable. An angular resolution of 0.55 arcsec should be realized on-axis. At full-field-of-view, an angular resolution of 0.69 arcsec should be achieved.

### (3.9) Solar Image

On June 3, 1993 at 11:00 A.M. (1600 UT) the 28 inch heliostat was used to reflect sunlight into the lab. The heliostat's sun-tracker was used to direct the sun into the 30 cm Cassegrain telescope. The sun-tracker controls allowed Active Region 7515 (see Fig. 26) to be placed in the center of the EXVM's field of view. Figure 27 is an image of this region obtained with the

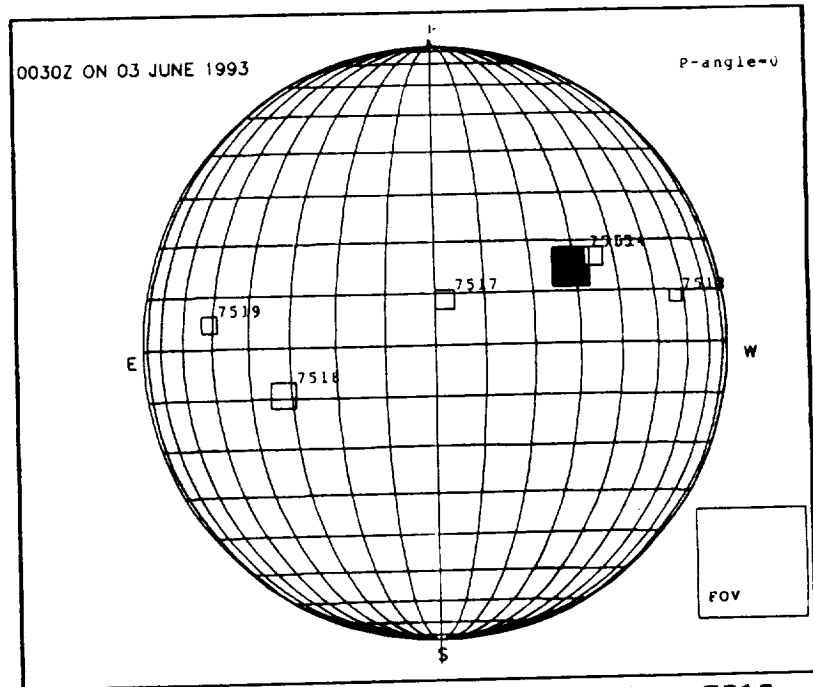


**Figure 26** The shaded region is Active Area 7515.

currently operational MSFC Vector Magnetograph. Each pixel in Fig. 27 is 2.5 arcsec across.

The 525.0 nm prefilter and blocking filters were used in the EXVM. The polarimeter was not available. The four Thompson-CFS, TH 7896(A) CCD detector arrays were not available. Another (smaller) CCD owned by the lab was placed at the image plane of the EXVM. The Fabry-Perot blocked too much light for this detector, and was not used.

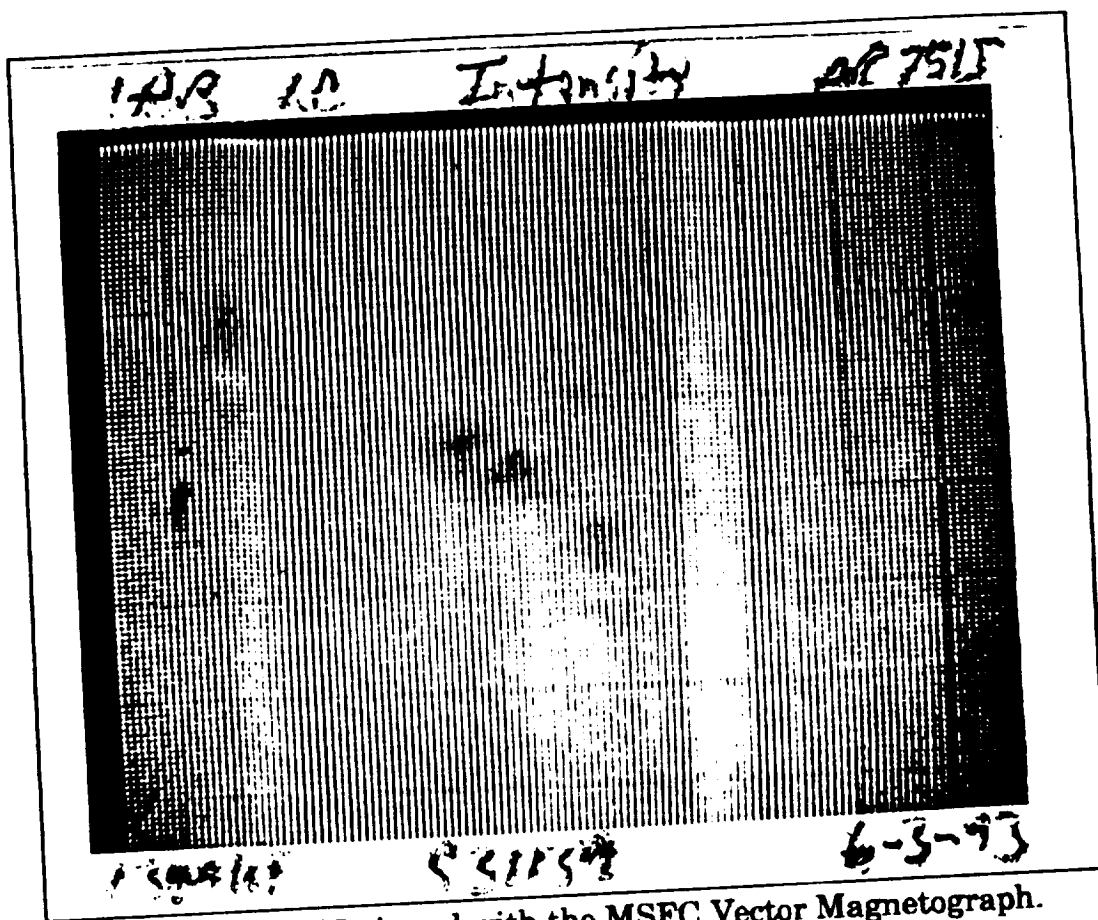
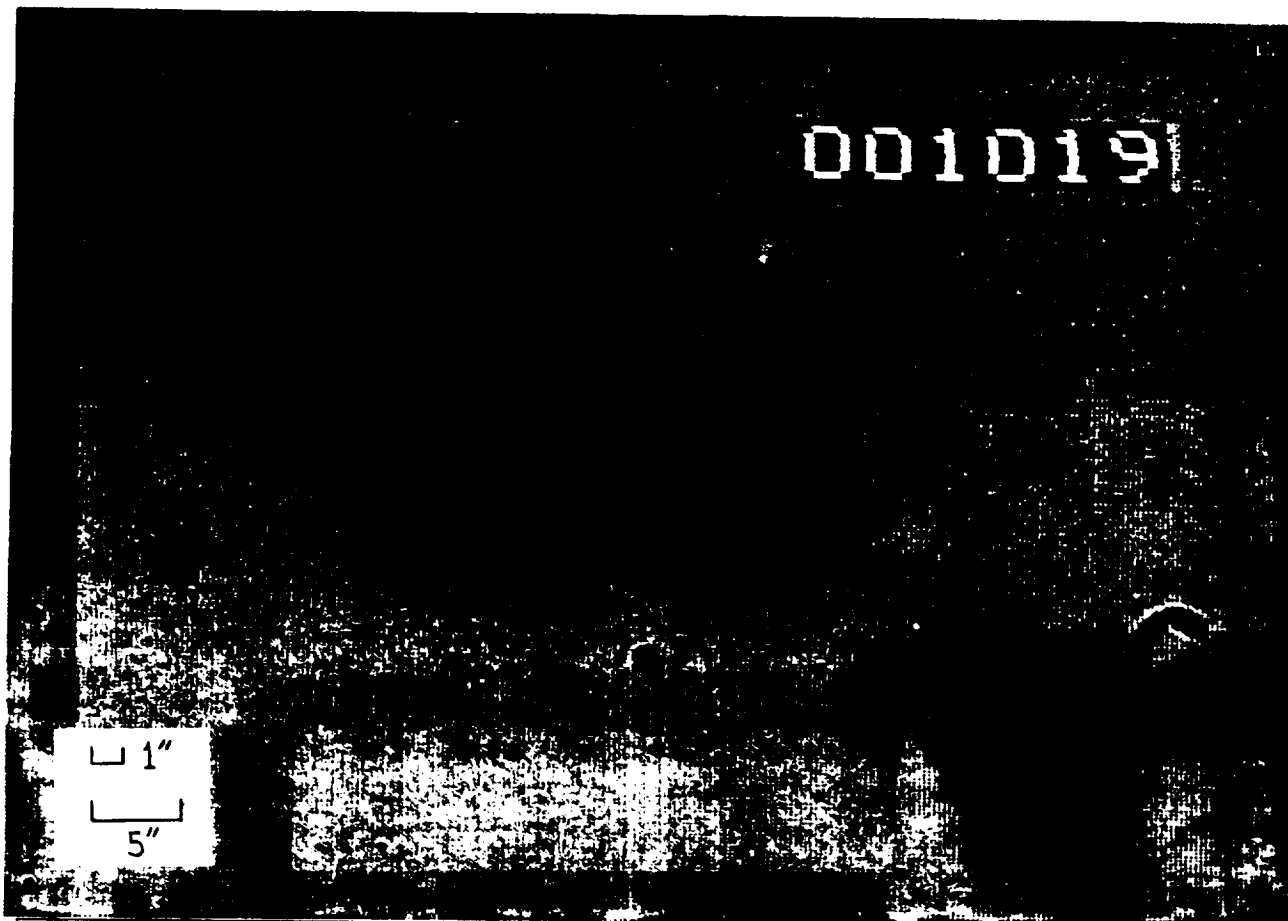


Figure 27 AR 7515 viewed with the MSFC Vector Magnetograph.

The output from the CCD detector placed at the image plane of the EXVM was recorded on videotape. The image bounced around due to wind striking the heliostat, but the sunspots remained in the field of view. Also, since the beam was being reflected horizontally across nearly 50 ft. of concrete, thermal fluctuations caused the seeing to vacillate wildly. The videotape was examined frame-by-frame, and a hardcopy was made of a frame having the best resolution attainable (see Fig. 28). This figure represents only a fraction of the EXVM's entire field of view. The small, well defined dark specs

in Fig. 28 are dust particles on the 15° dissector mirror and CCD camera, *not* sunspots.

Some definition was lost during image reproduction.



**Figure 28** An image of Active Region 7515 take on June 3, 1993 with the EXVM. A 28 inch heliostat (mirror) was used to reflect sunlight into the bread-boarded EXVM.

Using the known pixel size of Fig. 27, a scale for Fig. 28 was created. From this scale, it appears that a resolution of about 1 arcsec was achieved with the EXVM. Once the EXVM is assembled in a light-tight box and the heliostat is no longer used, a 0.5 arcsec resolution should be realized.

#### **(4) Suggestions for Future Work**

The EXVM was designed with large collimated spaces and telecentric spaces. A great deal of flexibility is provided for experimentation with polarimeter, blocking filter, and Fabry-Perot locations. Once the optimum positions are determined, the  $y-\bar{y}$  diagram can be modified to decrease the overall length of future systems.

Once the polarimeter is ready, it should be placed in the EXVM. An inactive (and presumably non-polarized) region of the sun should be observed. Rotating the polarimeter and observing the periodic variations of intensity at the image plane will provide an accurate measurement of instrumental polarization.

## REFERENCES

- <sup>1</sup>D. Malacara, Optical Shop Testing, 2nd ed. (Wiley, New York, 1992), pp. 123-166.
- <sup>2</sup>L. Baker, Selected Papers on Optical Transfer Function: Measurement, (SPIE Optical Engineering Press, Bellingham, WA, 1992).
- <sup>3</sup>D. Malacara, Selected Papers on Optical Shop Metrology, (SPIE Optical Engineering Press, Bellingham, WA, 1992).
- <sup>4</sup>D. Malacara, Optical Shop Testing, pp. 270-280.
- <sup>5</sup>R. N. Smartt, "Special applications of the point-diffraction interferometer," SPIE Proceedings **192**, 35-40 (1979).
- <sup>6</sup>L. Rubin, "Scatterplate interferometry," Optical Engineering **19(6)**, 815-824 (Nov., Dec. 1980)
- <sup>7</sup>M.V.R.K. Murty, "Common path interferometer using Fresnel Zone Plates," J. Opt. Soc. Am. **53(3)**, 568-570 (May 1963)
- <sup>8</sup>R. N. Smartt, "Theory and application of point-diffraction interferometers," Japan J. Appl. Phys. **14**, Suppl. 14-1, 351-356 (1974).
- <sup>9</sup>R. N. Smartt (1979).
- <sup>10</sup>R. N. Smartt (1979).
- <sup>11</sup>R. N. Smartt (1974).
- <sup>12</sup>D. Malacara, Optical Shop Testing, pp. 86-87.
- <sup>13</sup>C. S. Williams and O. A. Bechlund, Introduction to the Optical Transfer Function, (Wiley, New York, 1989), p. 322.

<sup>14</sup>R. Kingslake, "The interferometer patterns due to the primary aberrations," Trans. Opt. Soc., **27**, 94-105 (1925-1926).

<sup>15</sup>D. Malacara, Optical Shop Testing, pp. 77-86.

<sup>16</sup>C. S. Williams and O. A. Bechlund, Introduction to the Optical Transfer Function, Appendix A.

<sup>17</sup>C. S. Williams and O. A. Bechlund, Introduction to the Optical Transfer Function, p. 354.



This is a non-rotationally symmetric system  
 first order properties and third order quantities derived from them are  
 probably inadequate in describing system characteristics and performance.

close aperture on s53

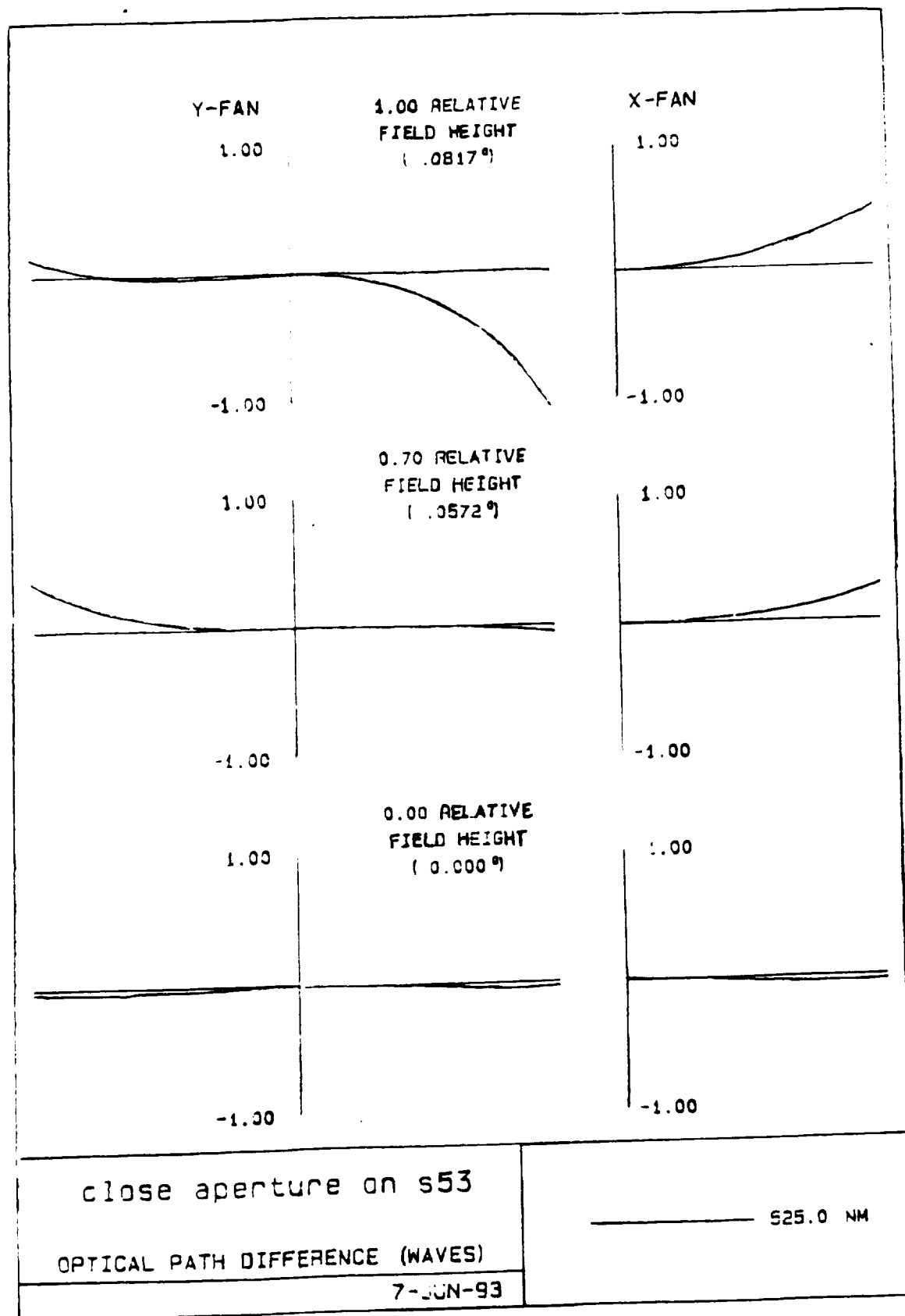
Position 1, Wavelength = 525.0 NM

|                | ( P )<br>HMY | ( U )<br>UMY | N * IMY   | ( P )<br>HCY | ( U )<br>UCY | N * ICY   |
|----------------|--------------|--------------|-----------|--------------|--------------|-----------|
| EP 152.400000  | 0.000000     |              |           | 0.000000     | 0.001425     |           |
| 1 152.400000   | 0.000000     | 0.000000     | 0.000000  | -0.926518    | 0.000938     | 0.001425  |
| 2 152.400000   | 0.000000     | 0.000000     | 0.000000  | -0.926517    | 0.001425     | 0.001425  |
| STO 152.400000 | 0.127279     | -0.063640    | -0.063640 | 0.000000     | -0.001425    | 0.001425  |
| 4 40.745715    | -0.032327    | -0.079803    | -0.079803 | 1.250428     | 0.004339     | 0.002882  |
| 5 6.187768     | -0.021270    | -0.032327    | -0.032327 | 5.889186     | 0.002855     | 0.004339  |
| 6 6.038879     | -0.032327    | -0.032327    | -0.032327 | 5.909172     | 0.004339     | 0.004339  |
| 7 5.877242     | -0.021270    | -0.032327    | -0.032327 | 5.930868     | 0.002855     | 0.004339  |
| 8 4.813749     | -0.032327    | -0.032327    | -0.032327 | 6.073623     | 0.004339     | 0.004339  |
| 9 4.652112     | -0.021270    | -0.032327    | -0.032327 | 6.095319     | 0.002855     | 0.004339  |
| 10 4.524493    | -0.032327    | -0.032327    | -0.032327 | 6.112450     | 0.004339     | 0.004339  |
| 11 4.362856    | -0.021270    | -0.032327    | -0.032327 | 6.134146     | 0.002855     | 0.004339  |
| 12 4.213967    | -0.032327    | -0.032327    | -0.032327 | 6.154132     | 0.004339     | 0.004339  |
| 13 4.052330    | -0.021270    | -0.032327    | -0.032327 | 6.175829     | 0.002855     | 0.004339  |
| 14 3.988520    | -0.032327    | -0.032327    | -0.032327 | 6.184394     | 0.004339     | 0.004339  |
| 15 -6.194598   | -0.015503    | -0.040950    | -0.040950 | 7.551287     | -0.001762    | 0.014851  |
| 16 -6.256610   | -0.019362    | -0.140837    | -0.140837 | 7.544239     | 0.001940     | 0.135101  |
| 17 -6.384400   | -0.000403    | 0.049444     | 0.049444  | 7.557043     | -0.033548    | -0.092551 |
| 18 -6.426724   | -0.000265    | -0.000403    | -0.000403 | 4.034458     | -0.022073    | -0.033548 |
| 19 -6.506285   | -0.000403    | -0.000403    | -0.000403 | -2.587524    | -0.033548    | -0.033548 |
| 20 -6.519789   | 0.011009     | -0.031339    | -0.031339 | -3.711396    | -0.014919    | -0.051159 |
| 21 -6.464743   | 0.008406     | 0.142385     | 0.142385  | -3.785991    | -0.015829    | 0.049783  |
| 22 -6.427755   | 0.021331     | 0.033797     | 0.033797  | -3.855639    | -0.021001    | -0.013523 |
| 23 -4.327902   | -0.021331    | 0.021331     | 0.021331  | -5.430683    | 0.021001     | -0.021001 |
| 24 -2.078715   | -0.006732    | 0.036048     | 0.036048  | -8.137238    | 0.035827     | 0.036608  |
| 25 -2.046401   | -0.012020    | 0.084004     | 0.084004  | -8.309207    | 0.021038     | 0.234937  |
| 26 -2.010341   | -0.001344    | -0.031214    | -0.031214 | -8.372319    | 0.102462     | -0.238051 |
| 27 -1.990187   | -0.000884    | 0.001344     | 0.001344  | -9.909252    | 0.067415     | -0.102462 |
| 28 -1.990196   | -0.001344    | 0.001344     | 0.001344  | -9.908578    | 0.102462     | -0.102462 |
| 29 -1.925704   | -0.000884    | 0.001344     | 0.001344  | -14.826762   | 0.067415     | -0.102462 |
| 30 -1.922168   | -0.001344    | 0.001344     | 0.001344  | -15.096423   | 0.102462     | -0.102462 |
| 31 -1.857677   | -0.000884    | 0.001344     | 0.001344  | -20.014606   | 0.067415     | -0.102462 |
| 32 -1.857685   | -0.001344    | 0.001344     | 0.001344  | -20.013932   | 0.102462     | -0.102462 |
| 33 -1.707182   | -0.003984    | -0.007720    | -0.007720 | -31.491437   | 0.010229     | -0.269650 |
| 34 -1.657381   | -0.002464    | 0.024146     | 0.024146  | -31.619301   | 0.030977     | 0.329592  |
| 35 -1.642596   | -0.006831    | 0.010783     | 0.010783  | -31.805163   | -0.000019    | 0.076535  |

TABLE A1. Paraxial ray trace of the EXVM. HMY and UMY are the marginal ray height and angle. HCY and UCY are chief ray quantities. (IMY and ICY are marginal and chief ray angles of incidence.) Each quantity is calculated at every surface of the EXVM, as listed in TABLE 1, page 3.

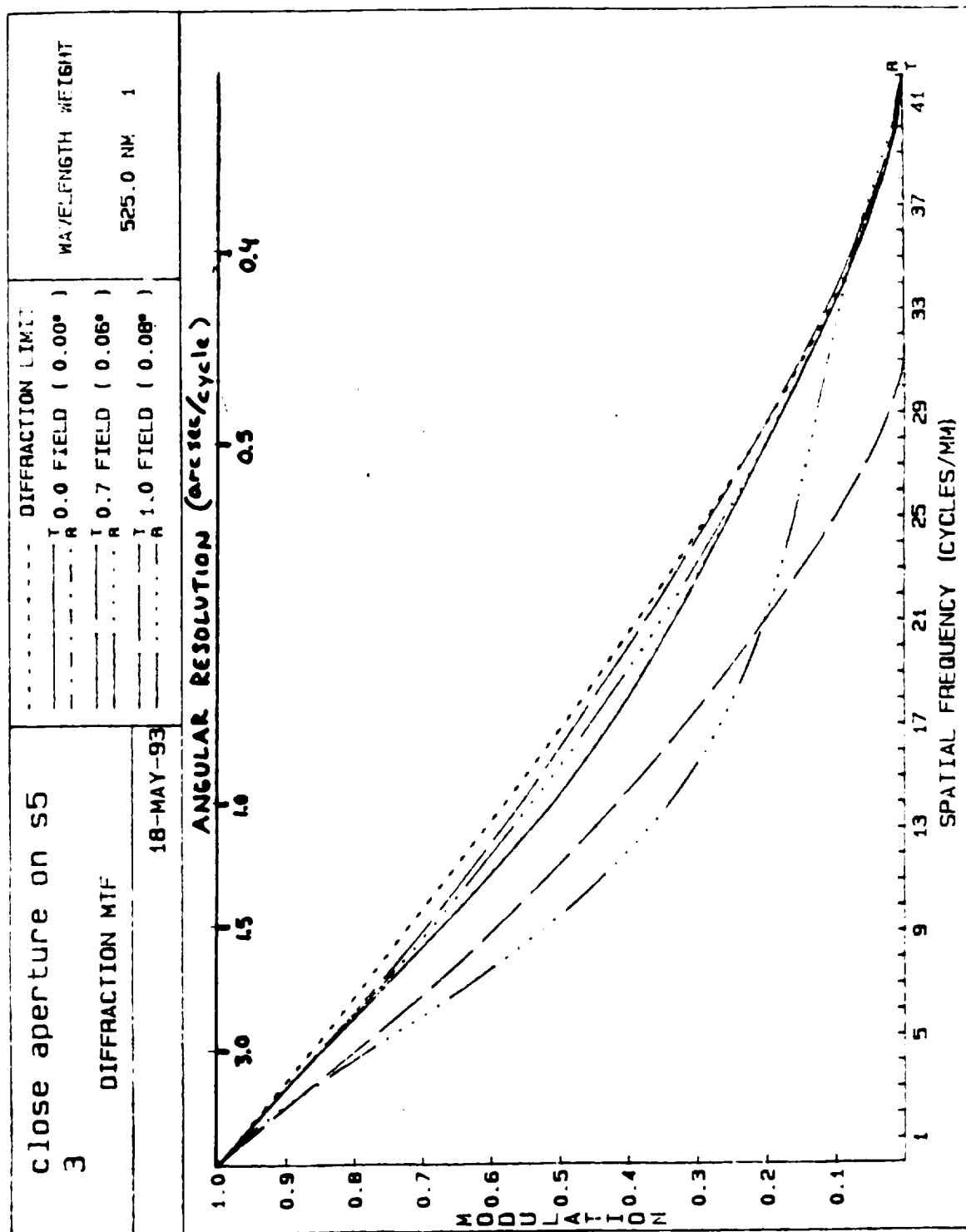
|     |           |           |           |            |           |           |
|-----|-----------|-----------|-----------|------------|-----------|-----------|
| 36  | -1.266885 | 0.006831  | 0.006831  | -31.804096 | 0.000019  | 0.000019  |
| 37  | -0.138158 | 0.004495  | 0.006831  | -31.800888 | 0.000013  | 0.000019  |
| 38  | -0.120180 | 0.006831  | 0.006831  | -31.800837 | 0.000019  | 0.000019  |
| 39  | -0.038206 | 0.004495  | 0.006831  | -31.800604 | 0.000013  | 0.000019  |
| 40  | 0.056179  | 0.006831  | 0.006831  | -31.800336 | 0.000019  | 0.000019  |
| 41  | 0.056181  | 0.004495  | 0.006831  | -31.800336 | 0.000013  | 0.000019  |
| 42  | 0.137083  | 0.006831  | 0.006831  | -31.800106 | 0.000019  | 0.000019  |
| 43  | 0.137083  | 0.004495  | 0.006831  | -31.800106 | 0.000013  | 0.000019  |
| 44  | 0.231468  | 0.006831  | 0.006831  | -31.799838 | 0.000019  | 0.000019  |
| 45  | 0.313442  | 0.004495  | 0.006831  | -31.799605 | 0.000013  | 0.000019  |
| 46  | 0.331420  | 0.006831  | 0.006831  | -31.799554 | 0.000019  | 0.000019  |
| 47  | 0.877909  | 0.003536  | 0.008135  | -31.798001 | 0.019142  | -0.047217 |
| 48  | 0.899127  | 0.004338  | 0.012742  | -31.683148 | 0.006086  | -0.207397 |
| 49  | 0.942511  | 0.004976  | 0.001864  | -31.622283 | 0.063529  | 0.167938  |
| 50  | 3.127019  | -0.005514 | 0.030668  | -3.732943  | 0.052290  | 0.032859  |
| 51  | 3.106067  | -0.001674 | -0.060999 | -3.534241  | 0.043518  | 0.139346  |
| 52  | 3.101882  | -0.010687 | -0.022254 | -3.425446  | 0.081834  | 0.094608  |
| 53  | 1.701589  | -0.025971 | 0.042223  | 7.297245   | -0.029926 | 0.308739  |
| 54  | 1.585757  | -0.019463 | -0.151320 | 7.163775   | -0.006418 | -0.546608 |
| 55  | 1.556562  | -0.044568 | -0.061987 | 7.154148   | -0.065280 | -0.145340 |
| 56  | 0.000000  | 0.044568  | -0.044568 | 4.874194   | 0.065280  | -0.065280 |
| 57  | -5.385824 | 0.014580  | -0.074044 | -3.014621  | 0.032160  | -0.081779 |
| 58  | -5.414985 | 0.024355  | -0.227285 | -3.078942  | 0.030443  | -0.169350 |
| 59  | -5.531890 | -0.010837 | 0.097219  | -3.268270  | 0.032867  | 0.019168  |
| 60  | -4.751638 | 0.010837  | 0.010837  | -5.634672  | -0.032867 | -0.032867 |
| 61  | -1.965719 | -0.010837 | 0.010837  | -14.083994 | 0.032867  | -0.032867 |
| 62  | -1.185466 | 0.010837  | 0.010837  | -16.450397 | -0.032867 | -0.032867 |
| IMG | -0.015088 | 0.010837  |           | -20.000000 | -0.032867 |           |

ORIGINAL PAGE IS  
OF POOR QUALITY



ORIGINAL PAGE IS  
OF POOR QUALITY

**FIGURE A1.** Wavefront aberrations (measured in waves) of the EXVM plotted for the center, 70% of maximum, and 100% of the full field-of-view. All curves are calculated for a wavelength of 525.0 nm.



ORIGINAL PAGE IS  
OF POOR QUALITY

**FIGURE A2.** The diffraction MTF for the EXVM. The MTF is given in arcseconds per cycle and in cycles per mm (at the image plane) for objects at 0%, 70%, and 100% of full field-of-view.

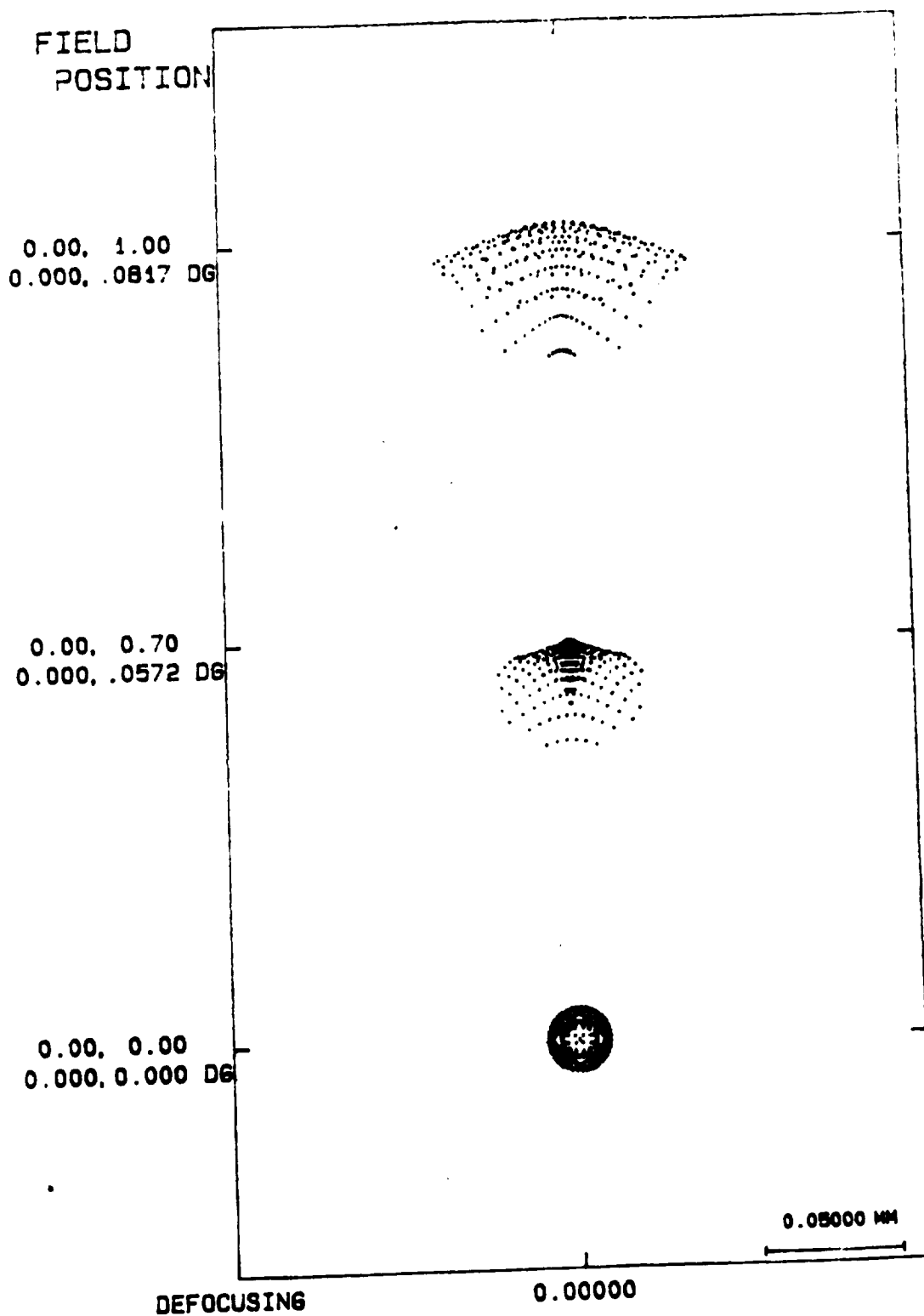


**FIGURE A3.** Spot diagrams of the EXVM calculated at 0%, 70%, and 100% of the full field-of-view.

SPO

Univ of Alabama 18-MAY-93 12H 15M 26S  
CODE V VAX Version: 7.51 A

S P O T D I A G R A M A N A L Y S I S

---

| WAVELENGTH | WEIGHT | POINTS<br>TRACED | POINTS<br>ATTEMPTED |
|------------|--------|------------------|---------------------|
| 525.0      | 99     | 158              | 179                 |

Field 1, ( 0.00, 0.00) degrees. Focus 0.00000  
Displacement of centroid from chief ray  
X: 0.00000E+00 Y: -0.42018E-14

RMS spot diameter  
0.18807E-01 MM

Field 2, ( 0.00, 0.06) degrees. Focus 0.00000  
Displacement of centroid from chief ray  
X: 0.00000E+00 Y: -0.98896E-02

RMS spot diameter  
0.25141E-01 MM

Field 3, ( 0.00, 0.08) degrees. Focus 0.00000  
Displacement of centroid from chief ray  
X: 0.00000E+00 Y: -0.87191E-02

RMS spot diameter  
0.47644E-01 MM

**TABLE A2.** RMS spot size diameters calculated at 0%, 70%, and 100% of the full field-of-view.

WAV

Univ of Alabama 18-MAY-93 12H 14M 11S  
CODE V VAX Version: 7.51 A

## WAVEFRONT ANALYSIS

close aperture on s53

POSITION 1

|                |      |      |      |
|----------------|------|------|------|
| X REL. FIELD   | 0.00 | 0.00 | 0.00 |
| Y REL. FIELD   | 0.00 | 0.70 | 1.00 |
| WEIGHTS        | 1.00 | 0.88 | 0.50 |
| NUMBER OF RAYS | 308  | 310  | 244  |

|             |       |
|-------------|-------|
| WAVELENGTHS | 525.0 |
| WEIGHTS     | 1     |

| FIELD<br>FRACT | DEG  | SHIFT<br>(MM.) | BEST INDIVIDUAL FOCUS |                |        | SHIFT<br>(MM.) | BEST COMPOSITE FOCUS |                |        |
|----------------|------|----------------|-----------------------|----------------|--------|----------------|----------------------|----------------|--------|
|                |      |                | FOCUS<br>(MM.)        | RMS<br>(WAVES) | STREHL |                | FOCUS<br>(MM.)       | RMS<br>(WAVES) | STREHL |
| X 0.00         | 0.00 | 0.000000       | 1.465239              | 0.009          | 0.997  | 0.000000       | 0.000000             | 0.049          | 0.910  |
| Y 0.00         | 0.00 | 0.000000       |                       |                |        | 0.000000       |                      |                |        |
| X 0.00         | 0.00 | 0.000000       | -0.709026             | 0.034          | 0.957  | 0.000000       | 0.000000             | 0.041          | 0.936  |
| Y 0.70         | 0.06 | 0.032969       |                       |                |        | 0.018236       |                      |                |        |
| X 0.00         | 0.00 | 0.000000       | -2.415966             | 0.079          | 0.779  | 0.000000       | 0.000000             | 0.108          | 0.630  |
| Y 1.00         | 0.08 | 0.097282       |                       |                |        | 0.030064       |                      |                |        |

COMPOSITE RMS FOR  
POSITION 1: 0.061

Units of RMS are waves at 525.0 nm.

NOTE - Strehl is the intensity at the peak of the point image as a fraction of the peak of the aberration-free image with the same vignetting and obscuration. The approximation used here is generally valid for RMS < 0.1.

**TABLE A3.** The RMS wavefront deviation (measured in waves) of the EXVM. The best possible RMS deviation is calculated for each field-height. The best composite focus indicates a position that provides the best overall performance, averaged over all field heights.

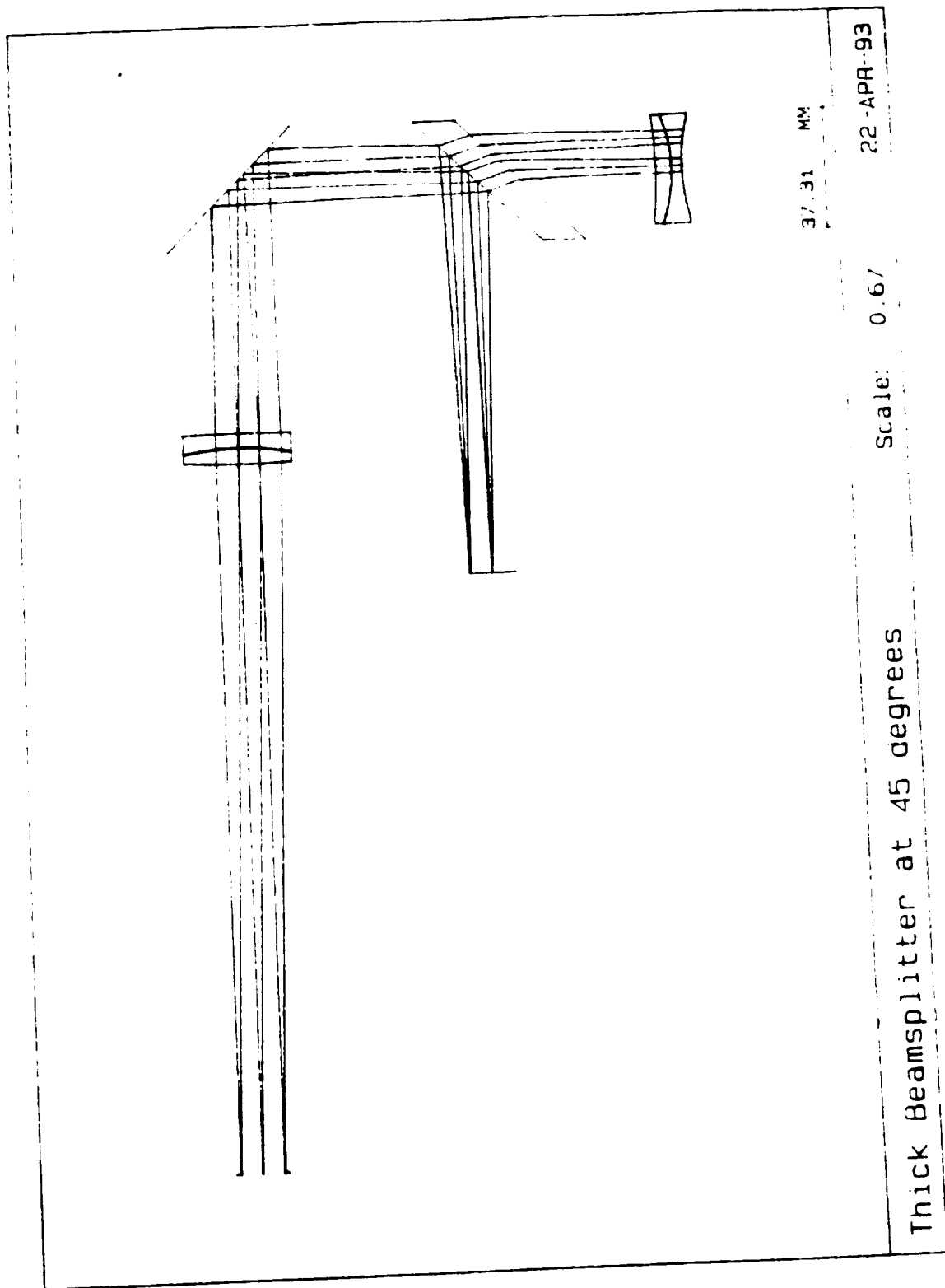
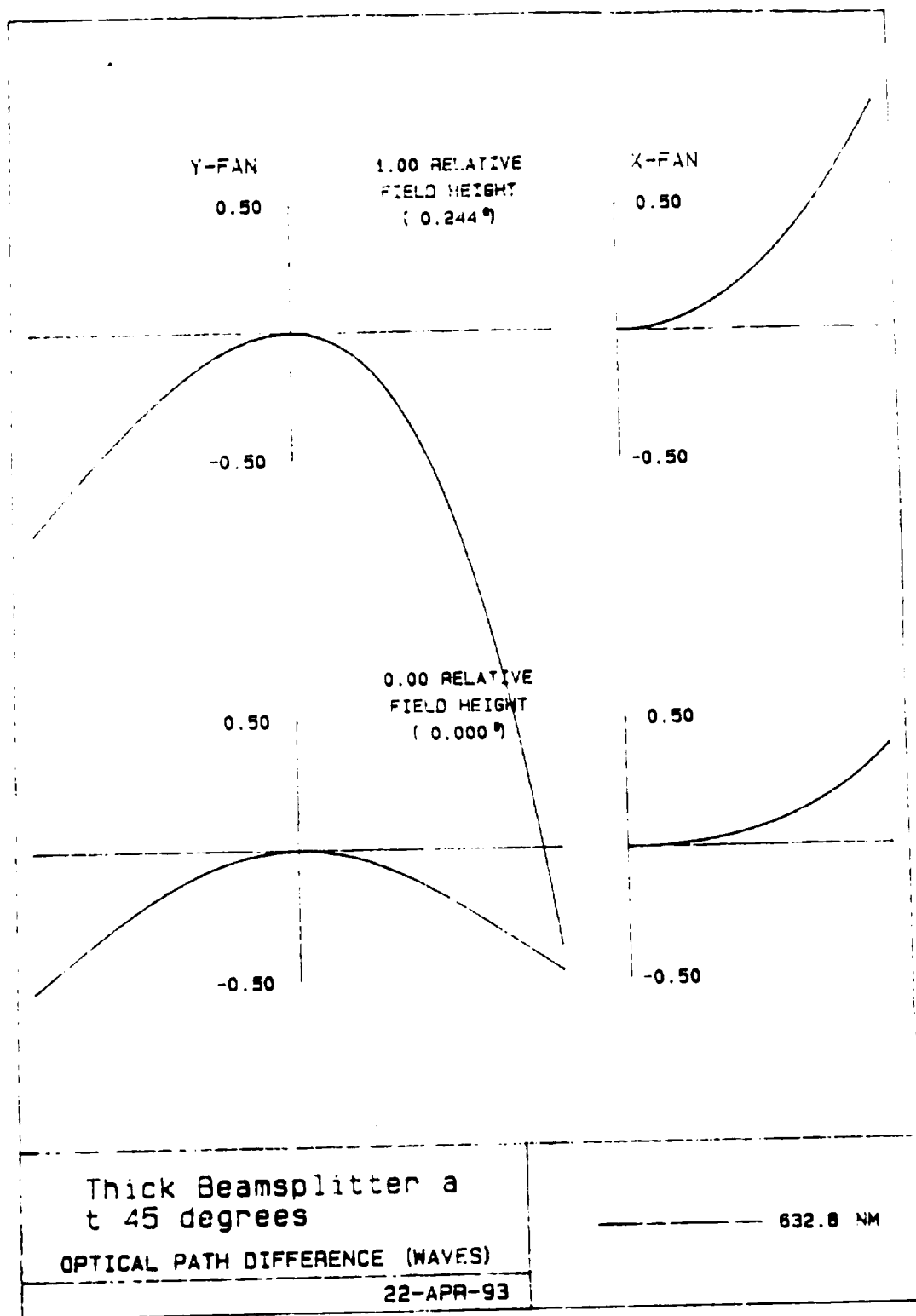


**FIGURE B1.** Partial drawing of the EXVM with a 1.57 cm thick beamsplitter inserted at 45°  
between lens #2 and lens #3.





ORIGINAL PAGE IS  
OF POOR QUALITY

**FIGURE B2.** Wavefront aberrations (measured in waves) of the EXVM with a 1.57 cm thick beamsplitter inserted at 45° between lens #2 and lens #3. All curves are calculated for a wavelength of 525.0 nm and plotted for the center and 100% of the full field-of-view.

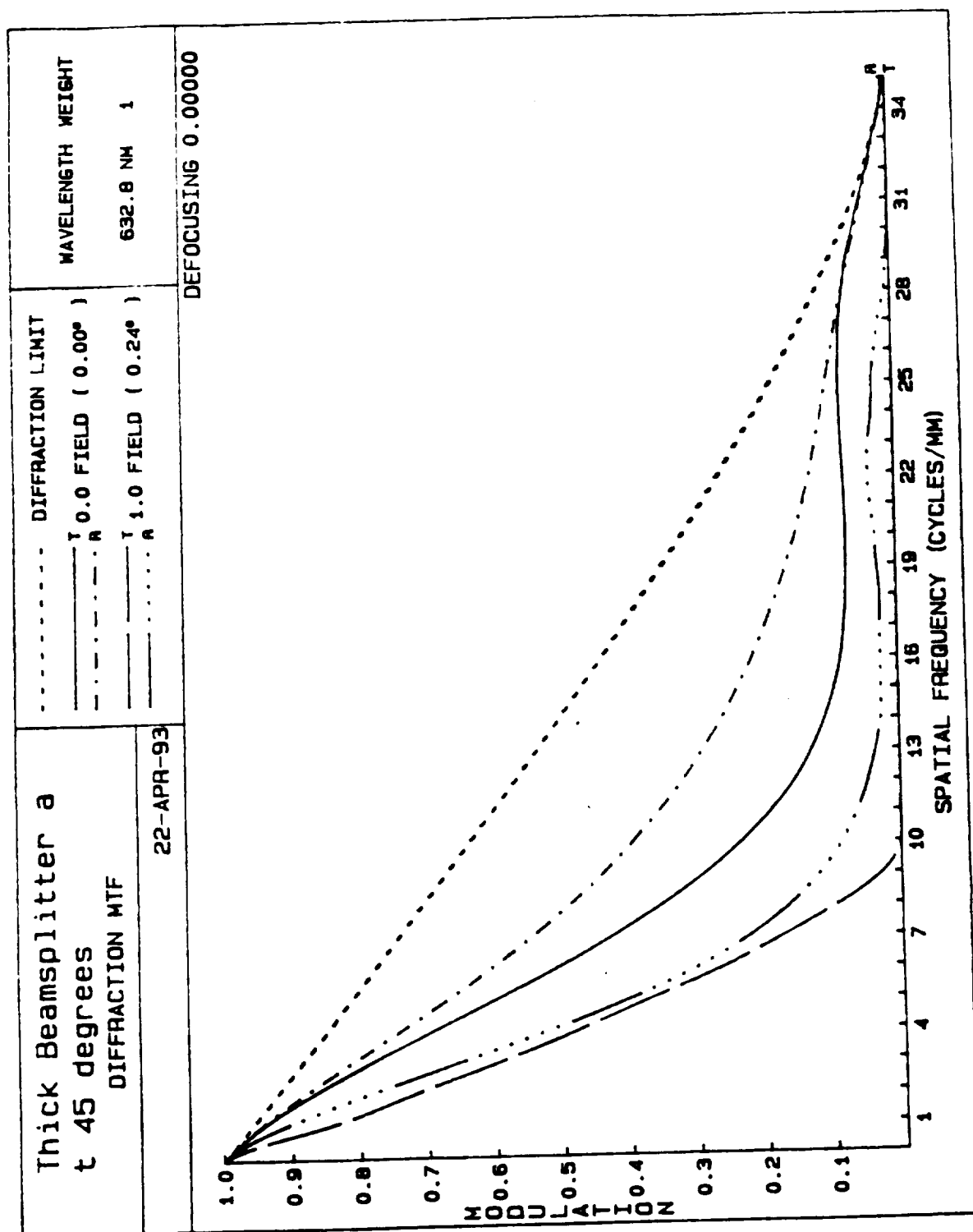


**FIGURE B3.** The diffraction MTF for the EXVM with a 1.57 cm thick beamsplitter inserted at 45° between lens #2 and lens #3. The MTF is given in arcseconds per cycle and in cycles per mm (at the image plane) for objects at 0% and 100% of full field-of-view.

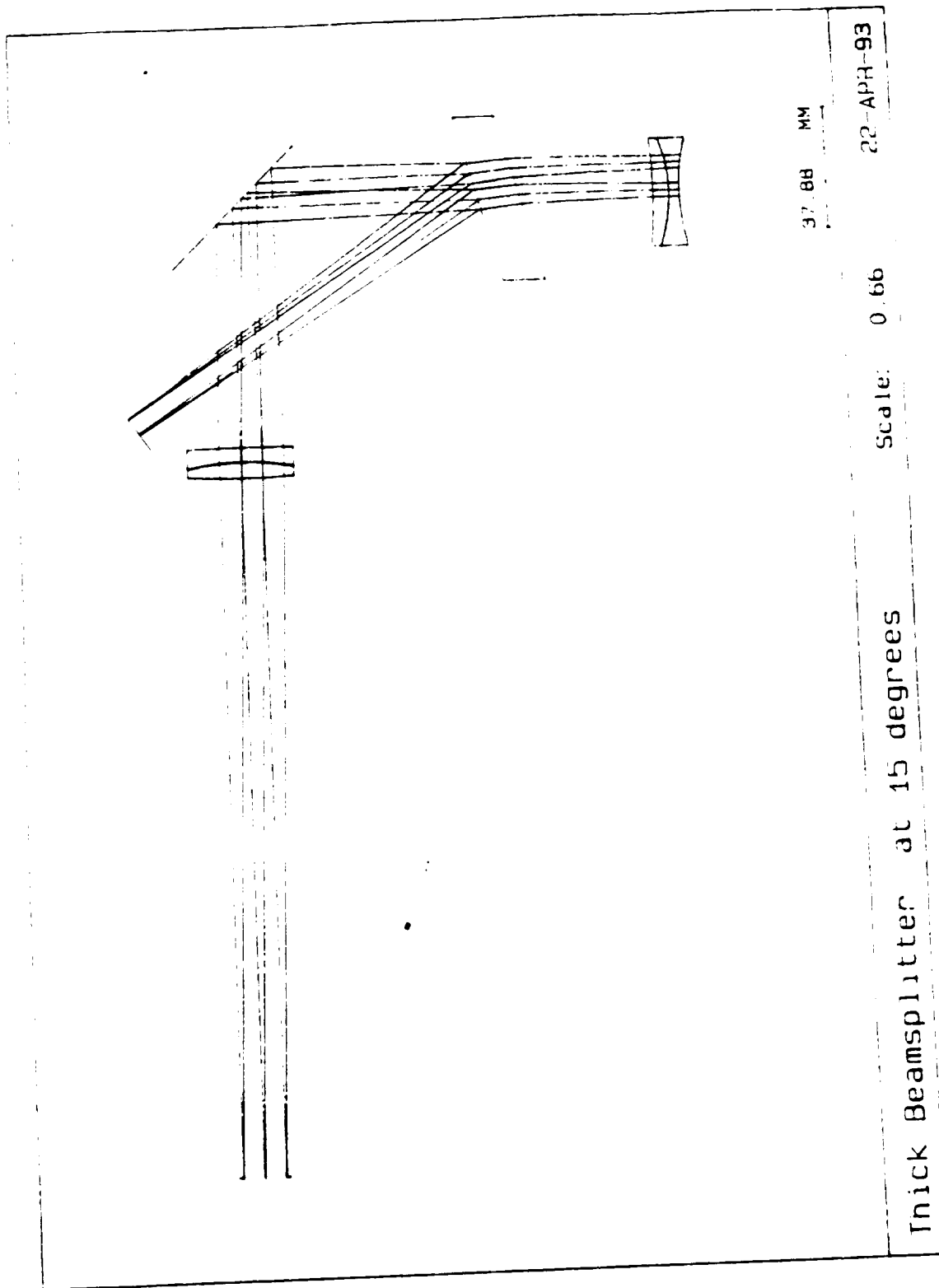
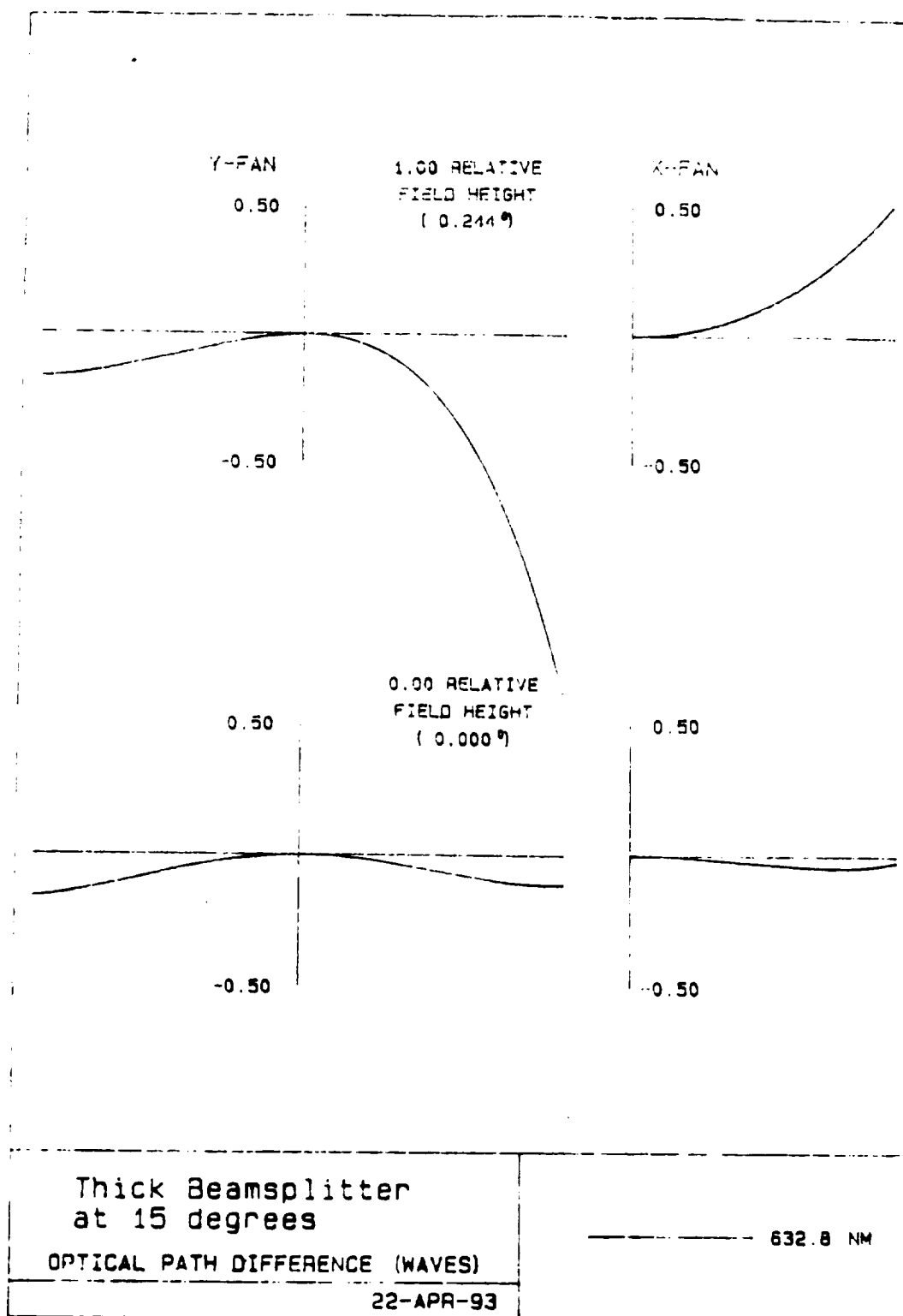


**FIGURE B4.** Partial drawing of the EXVM with a 1.57 cm thick beamsplitter inserted at 15° between lens #2 and lens #3

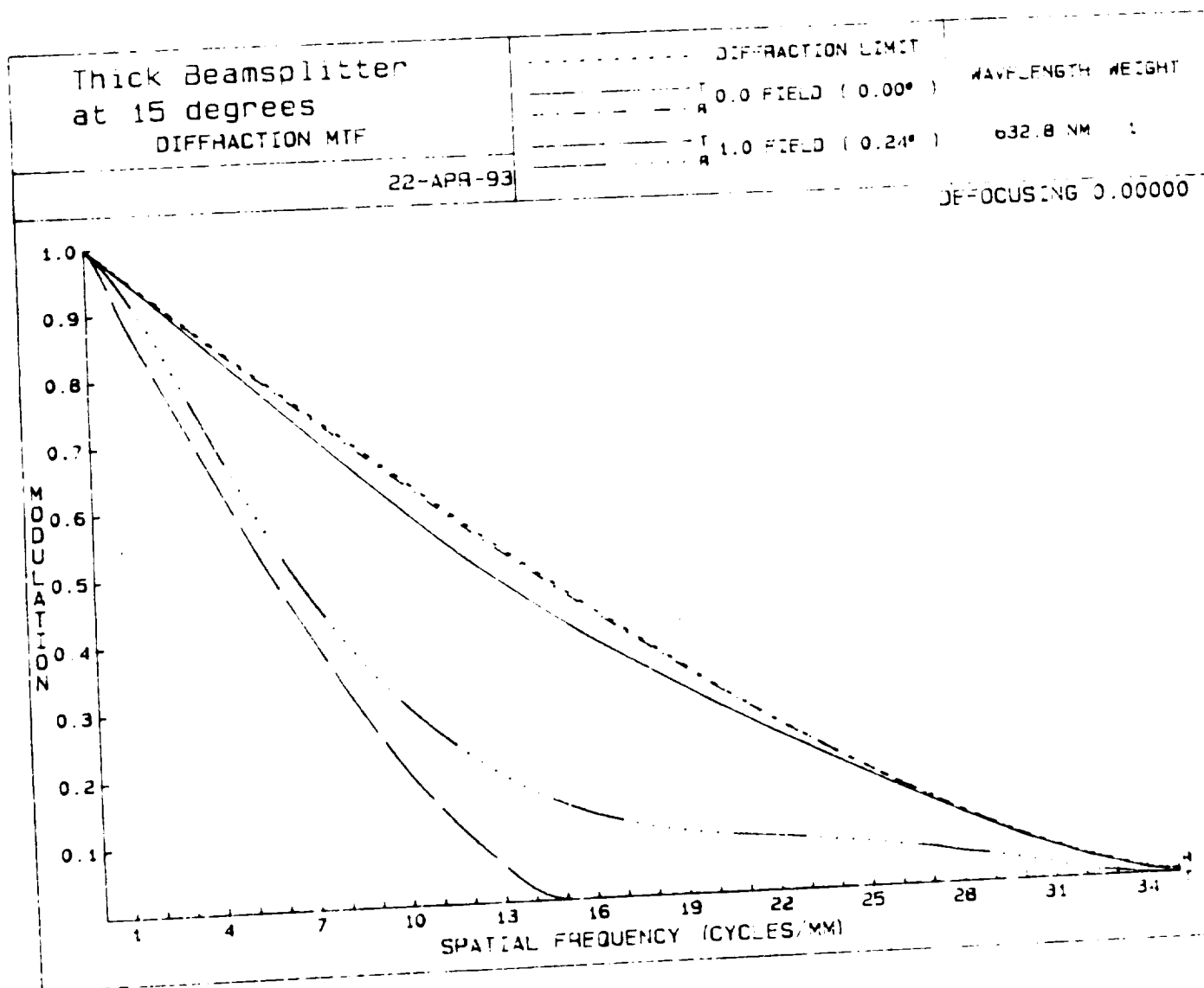
**Appendix B**

ORIGINAL PAGE IS  
OF POOR QUALITY



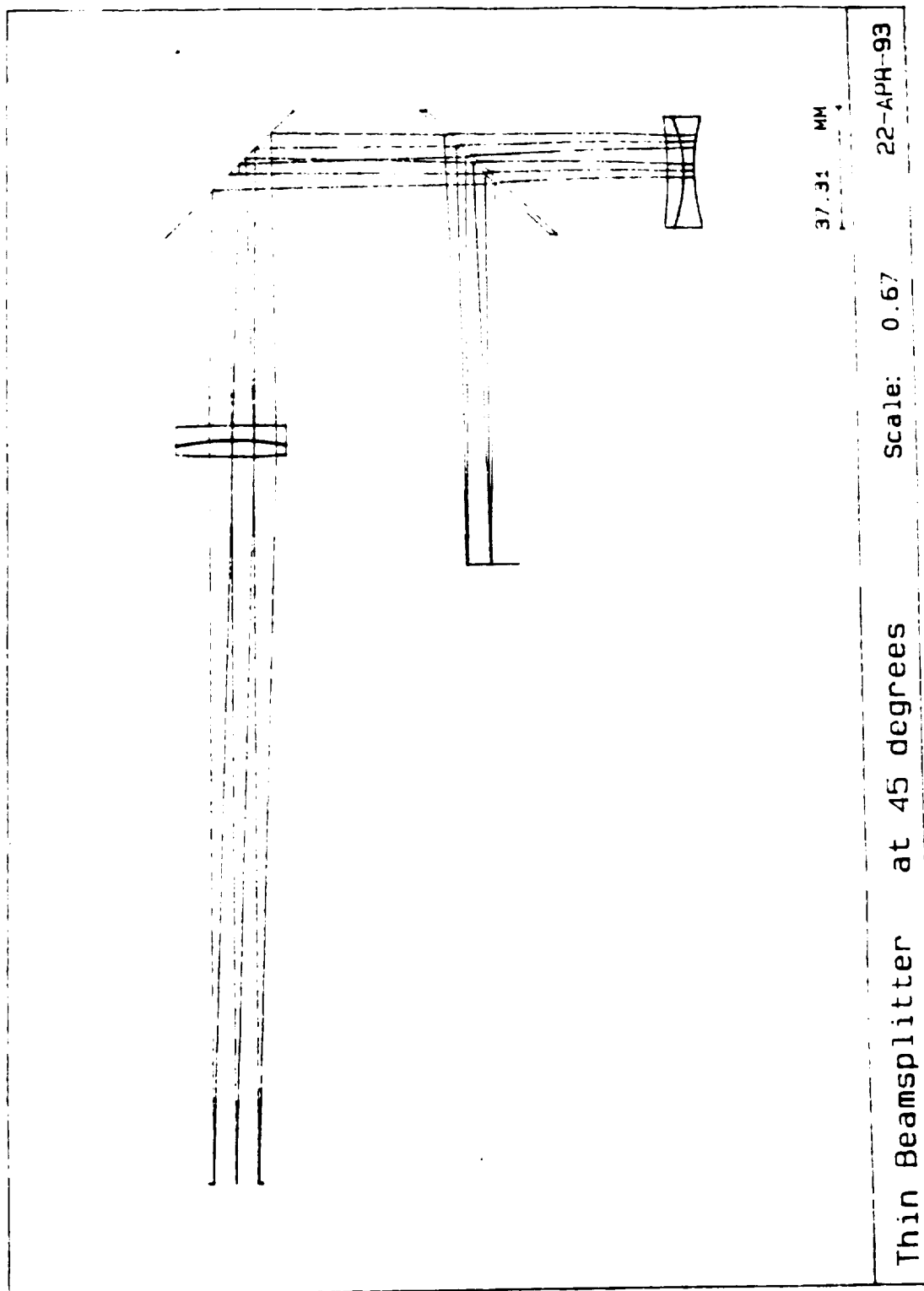
ORIGINAL PAGE IS  
OF POOR QUALITY

**FIGURE B5.** Wavefront aberrations (measured in waves) of the EXVM with a 1.57 cm thick beamsplitter inserted at 15° between lens #2 and lens #3. All curves are calculated for a wavelength of 525.0 nm and plotted for the center and 100% of the full field-of-view.



ORIGINAL PAGE IS  
OF POOR QUALITY

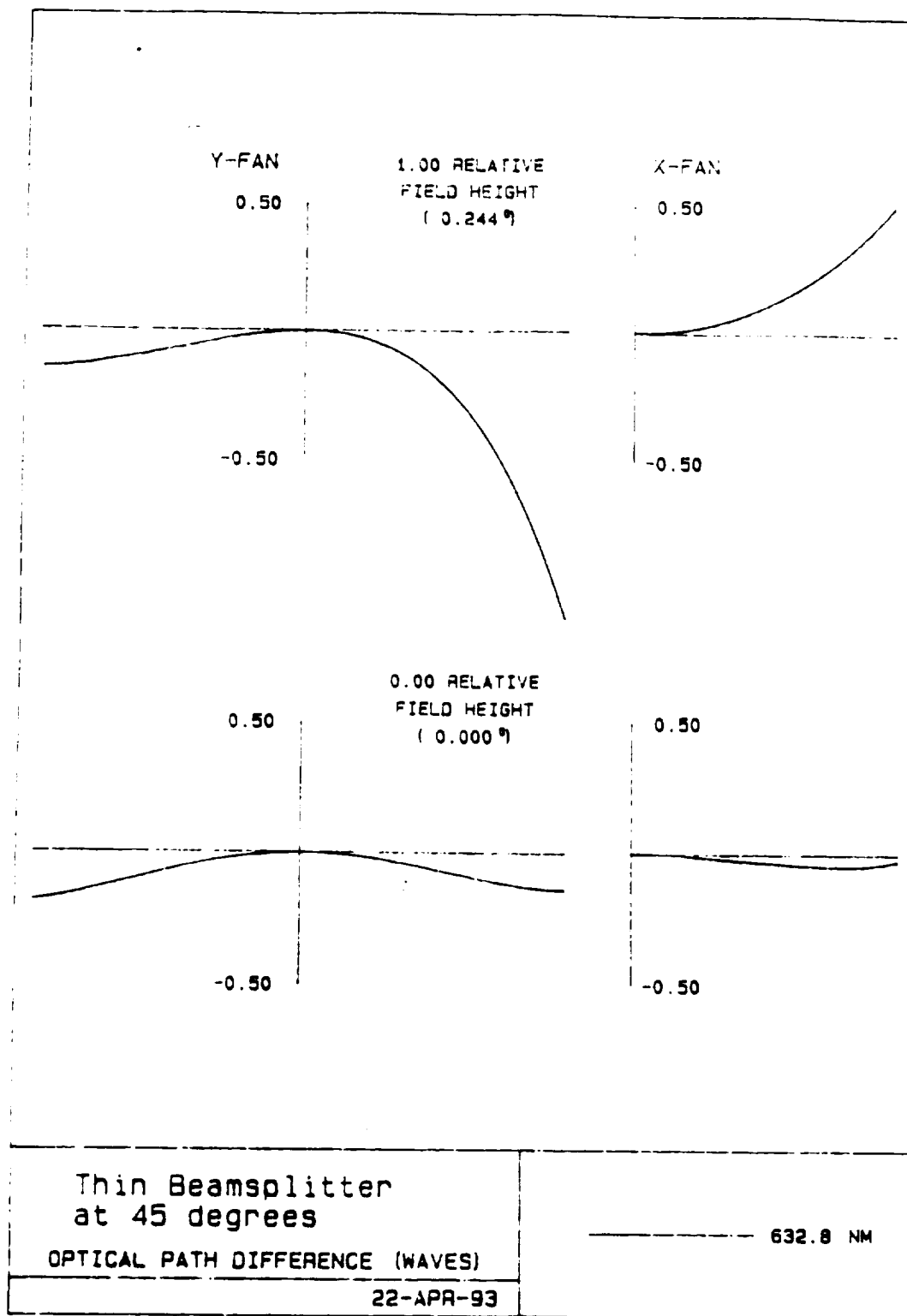
**FIGURE B6.** The diffraction MTF for the EXVM with a 1.57 cm thick beamsplitter inserted at 15° between lens #2 and lens #3. The MTF is given in arcseconds per cycle and in cycles per mm (at the image plane) for objects at 0% and 100% of full field-of-view.



ORIGINAL PAGE IS  
OF POOR QUALITY

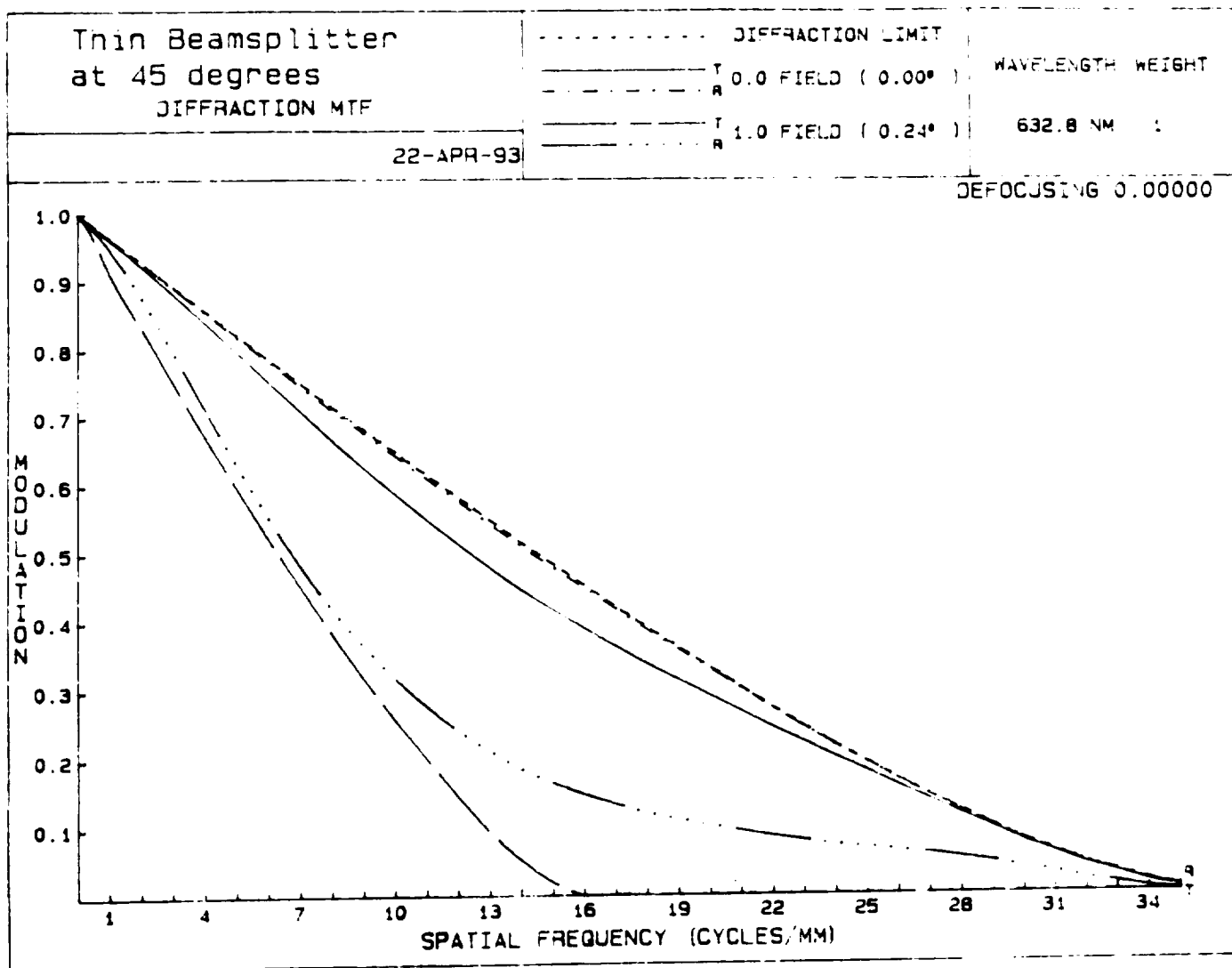
**FIGURE B7.** Partial drawing of the EXVM with a 2 mm thick beamsplitter inserted at 45° between lens #2 and lens #3

**Appendix B**



ORIGINAL PAGE IS  
OF POOR QUALITY

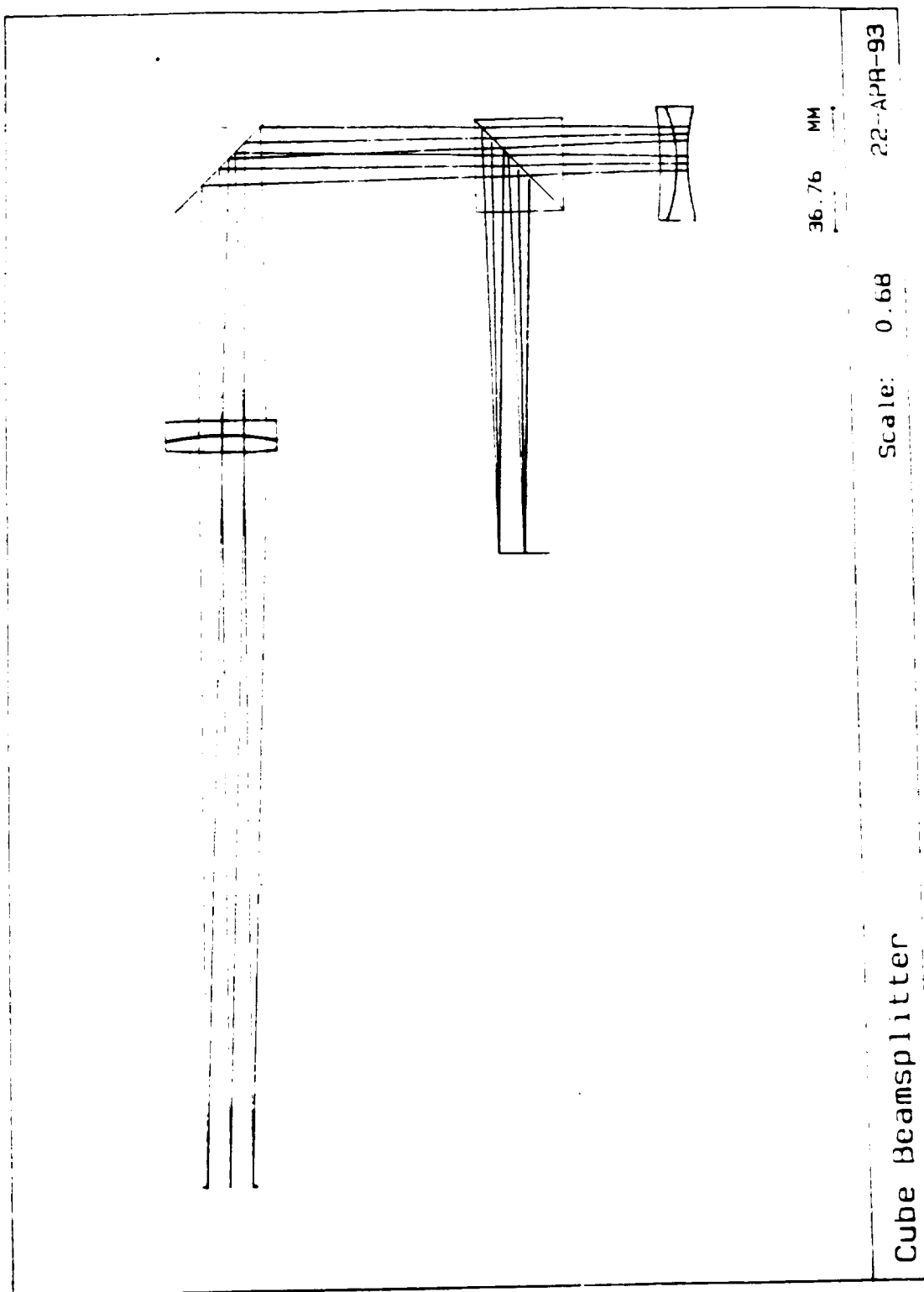
**FIGURE B8.** Wavefront aberrations (measured in waves) of the EXVM with a 2 mm thick beamsplitter inserted at 45° between lens #2 and lens #3. All curves are calculated for a wavelength of 525.0 nm and plotted for the center and 100% of the full field-of-view.



ORIGINAL PAGE IS  
OF POOR QUALITY

**FIGURE B9.** The diffraction MTF for the EXVM with a 2 mm thick beamsplitter inserted at 45° between lens #2 and lens #3. The MTF is given in arcseconds per cycle and in cycles per mm (at the image plane) for objects at 0% and 100% of full field-of-view.

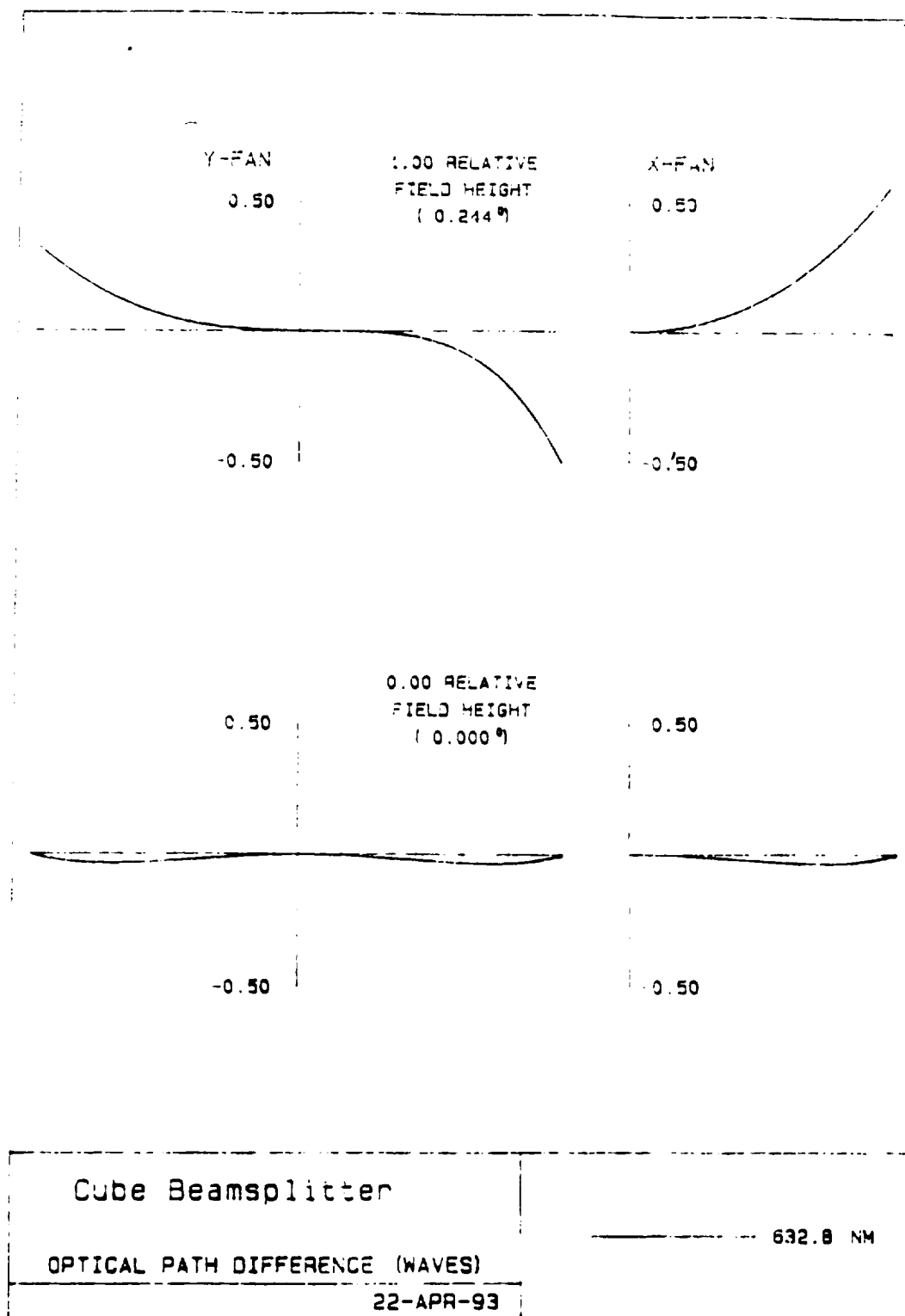




ORIGINAL PAGE IS  
OF POOR QUALITY

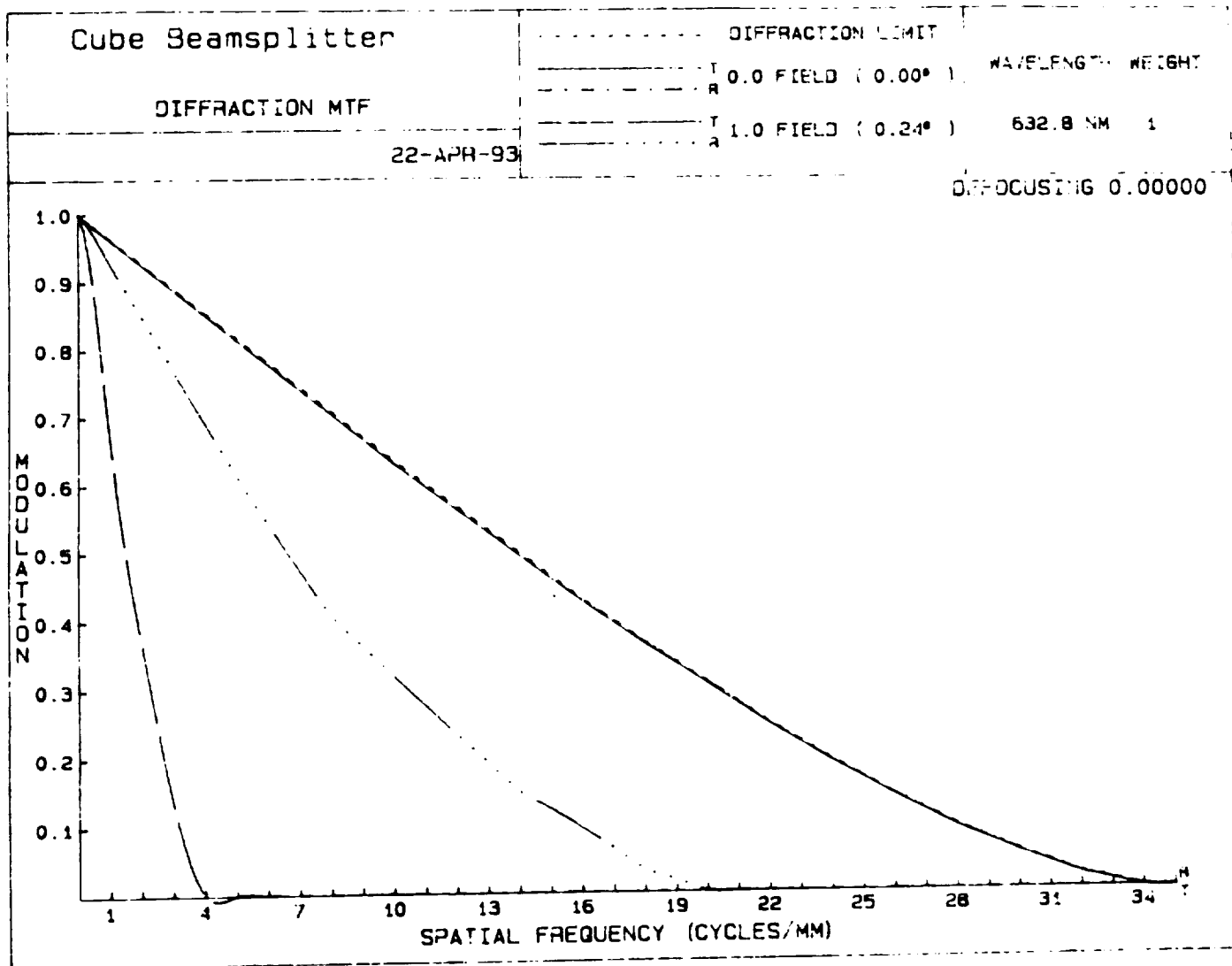
**FIGURE B10.** Partial drawing of the EXVM with a 2.54 inch cube beamsplitter inserted at 0° between lens #2 and lens #3

**Appendix B**



ORIGINAL PAGE IS  
OF POOR QUALITY

**FIGURE B11.** Wavefront aberrations (measured in waves) of the EXVM with a 2.54 cm cube beamsplitter inserted at 0° between lens #2 and lens #3. All curves are calculated for a wavelength of 525.0 nm and plotted for the center and 100% of the full field-of-view.



ORIGINAL PAGE IS  
OF POOR QUALITY

**FIGURE B12.** The diffraction MTF for the EXVM with a 2.54 cm cube beamsplitter inserted at 0° between lens #2 and lens #3. The MTF is given in arcseconds per cycle and in cycles per mm (at the image plane) for objects at 0% and 100% of full field-of-view.

# WAVELENGTH ANALYSIS

Thick Beamsplitter at 45 degrees

POSITION 1

X REL. FIELD 0.00 0.00  
Y REL. FIELD 0.00 1.00  
WEIGHTS 1.00 0.88  
NUMBER OF RAYS 110 70  
  
WAVELENGTHS 632.8  
WEIGHTS 1

| FIELD<br>FRACT | DEG  | SHIFT<br>(MM.) | BEST INDIVIDUAL FOCUS |                |        | SHIFT<br>(MM.) | BEST COMPOSITE FOCUS |                |        |
|----------------|------|----------------|-----------------------|----------------|--------|----------------|----------------------|----------------|--------|
|                |      |                | FOCUS<br>(MM.)        | RMS<br>(WAVES) | STREHL |                | FOCUS<br>(MM.)       | RMS<br>(WAVES) | STREHL |
| X 0.00         | 0.00 | 0.000000       | 0.433018              | 0.131          | 0.265  | 0.000000       | 0.083757             | 0.104          | 0.262  |
| Y 0.00         | 0.00 | 0.000364       |                       |                |        | 0.001471       |                      |                |        |
| X 0.00         | 0.00 | 0.000000       | 9.539810              | 0.026          | 0.974  | 0.000000       | 0.083757             | 0.119          | 0.418  |
| Y 1.00         | 0.24 | 0.016686       |                       |                |        | 0.069879       |                      |                |        |

COMPOSITE RMS FOR  
POSITION 1: 0.179

Units of RMS are waves at 632.8 nm.

NOTE - Strehl is the intensity at the peak of the point image as a fraction of the peak of the aberration free image with the same vignetting and obscuration. The approximation used here is generally valid for RMS < 0.1.

ORIGINAL PAGE IS  
OF POOR QUALITY

**TABLE B1.** The RMS wavefront deviation (measured in waves) of the EXVM with a 1.57 cm thick beamsplitter inserted at 45° between lens #2 and lens #3. The best possible RMS deviation is calculated for each field-height. The best composite focus indicates a position that provides the best overall performance, averaged over all field heights.

# WAVELENGTH ANALYSIS

Thick Beamsplitter at 15 degrees

POSITION 1

X REL. FIELD 0.00 0.00  
Y REL. FIELD 0.00 1.00  
WEIGHTS 1.00 0.88  
NUMBER OF RAYS 316 116  
WAVELENGTHS 632.8  
WEIGHTS 1

| FIELD<br>FRACT | DEG  | SHIFT<br>(MM.) | BEST INDIVIDUAL FOCUS |                |        | BEST COMPOSITE FOCUS |                |                |        |
|----------------|------|----------------|-----------------------|----------------|--------|----------------------|----------------|----------------|--------|
|                |      |                | FOCUS<br>(MM.)        | RMS<br>(WAVES) | STREHL | SHIFT<br>(MM.)       | FOCUS<br>(MM.) | RMS<br>(WAVES) | STREHL |
| X 0.00         | 0.00 | 0.000000       | 0.765168              | 0.027          | 0.973  | 0.000000             | 0.000739       | 0.035          | 0.954  |
| Y 0.00         | 0.00 | 0.000021       |                       |                |        | 0.000779             |                |                |        |
| X 0.00         | 0.00 | 0.000000       | 1.093492              | 0.018          | 0.937  | 0.000000             | 0.000739       | 0.103          | 0.664  |
| Y 1.00         | 0.24 | 0.140424       |                       |                |        | 0.020744             |                |                |        |

COMPOSITE RMS FOR  
POSITION 1: 0.058

Units of RMS are waves at 632.8 nm.

NOTE Strehl is the intensity at the peak of the point image as a fraction of the peak of the aberration free image with the same vignetting and obscuration. The approximation used here is generally valid for RMS < 0.1.

ORIGINAL PAGE IS  
OF POOR QUALITY

**TABLE B2.** The RMS wavefront deviation (measured in waves) of the EXVM with a 1.57 cm thick beamsplitter inserted at 15° between lens #2 and lens #3. The best possible RMS deviation is calculated for each field-height. The best composite focus indicates a position that provides the best overall performance, averaged over all field heights.

## Appendix B

# WAVELENGTH ANALYSIS

Cube Beamsplitter

POSITION 1

X REL. FIELD 0.00 0.00  
Y REL. FIELD 0.00 1.00  
WEIGHTS 1.00 0.88  
NUMBER OF RAYS 300 16  
WAVELENGTHS 632.8  
WEIGHTS 1

| FIELD<br>FRACT | DEG  | SHIFT<br>(MM.) | BEST INDIVIDUAL FOCUS<br>FOCUS<br>(MM.) | RMS<br>(WAVES) | STREHL | SHIFT<br>(MM.) | BEST COMPOSITE FOCUS<br>FOCUS<br>(MM.) | RMS<br>(WAVES)                   | STREHL |
|----------------|------|----------------|---|----------------|--------|----------------|--|----------------------------------|--------|
| X 0.00         | 0.00 | 0.000000       | 0.012442                                | 0.011          | 0.996  | 0.000000       | 0.000396                               | 0.011                            | 0.996  |
| Y 0.00         | 0.00 | 0.000000       |   |                |        | 0.000000       |  |                                  |        |
| X 0.00         | 0.00 | 0.000000       | 0.277633                                | 0.000          | 1.000  | 0.000000       | 0.000396                               | 0.001                            | 0.962  |
| Y 0.00         | 0.24 | 0.113415       |   |                |        | -0.023621      |  |                                  |        |
|                |      |                |   |                |        |                |  | COMPOSITE RMS FOR<br>POSITION 1: | 0.012  |

Units of RMS are waves at 632.8 nm.

NOTE - Strehl is the intensity at the peak of the point image as a fraction of the peak of the aberration free image with the same vignetting and obscuration. The approximation used here is generally valid for RMS < 0.1.

ORIGINAL PAGE IS  
OF POOR QUALITY

**TABLE B3.** The RMS wavefront deviation (measured in waves) of the EXVM with a 2 mm thick beamsplitter inserted at 45° between lens #2 and lens #3. The best possible RMS deviation is calculated for each field-height. The best composite focus indicates a position that provides the best overall performance, averaged over all field heights.

## Appendix B

# WAVELENGTH ANALYSIS

Thin Beamsplitter at 45 degrees

POSITION 1

X REL. FIELD 0.00 0.00  
Y REL. FIELD 0.00 1.00  
WEIGHTS 1.00 0.88  
NUMBER OF RAYS 516 132  
WAVELENGTHS 632.8  
WEIGHTS 1

| FIELD<br>FRAC                    | OCG  | SHIFT<br>(MM.) | BEST INDIVIDUAL FOCUS<br>FOCUS<br>(MM.) | RMS<br>(WAVES) | STREHL | SHIFT<br>(MM.) | BEST COMPOSITE FOCUS<br>FOCUS<br>(MM.) | RMS<br>(WAVES) | STREHL |
|----------------------------------|------|----------------|---|----------------|--------|----------------|--|----------------|--------|
| X 0.00                           | 0.00 | 0.000000       | 0.006674                                | 0.031          | 0.964  | 0.000000       | -0.000559                              | 0.041          | 0.937  |
| Y 0.00                           | 0.00 | 0.000059       |   |                |        | 0.000644       |  |                |        |
| X 0.00                           | 0.00 | 0.000000       | -4.718635                               | 0.024          | 0.977  | 0.000000       | 0.000559                               | 0.104          | 0.651  |
| Y 1.00                           | 0.24 | 0.129194       |   |                |        | 0.016414       |  |                |        |
| COMPOSITE RMS FOR<br>POSITION 1: |      |                |   |                |        |                |  | 0.064          |        |

Units of RMS are waves at 632.8 nm.

NOTE - Strehl is the intensity at the peak of the point image as a fraction of the peak of the aberration-free image with the rms vignetting and obscuration. The approximation used here is generally valid for RMS < 0.1.

OF POOR QUALITY

ORIGINAL PAGE IS  
OF POOR QUALITY

**TABLE B4.** The RMS wavefront deviation (measured in waves) of the EXVM with a 2.54 cm cube beamsplitter inserted at 0° between lens #2 and lens #3. The best possible RMS deviation is calculated for each field-height. The best composite focus indicates a position that provides the best overall performance, averaged over all field heights.

|   |  |  |  |
|---|--|--|--|
| To be initiated by the responsible NASA Project Officer, Technical Monitor, or other appropriate NASA official for all presentations, reports, papers, and proceedings that contain scientific and technical information. Explanations are on the back of this form and are presented in greater detail in NHB 2200.2, "NASA Scientific and Technical Information Handbook."  |  |  | (CASI Use Only)<br>Control No. _____<br>Date _____ |
| <b>I. DOCUMENT/PROJECT IDENTIFICATION</b> (Information contained on report documentation page should not be repeated except title, date and contract number)<br>Title: <u>Optical System Analysis for the ground based EXVM - Final Report</u><br>Author(s): <u>L. W. Hillman, R. A. Chipman, M. H. Smith</u><br>Original NASA Organization: <u>MSFC</u><br>Performing Organization (if different): <u>The University of Alabama in Huntsville</u><br>Contract/Grant/Agency/Project Number(s): <u>NAS8-38609, D. O. #46</u><br>Document Number(s): <u>NASA CR-192588</u><br>Document Date: <u>6/30/93</u><br>(For presentations or externally published documents, enter appropriate information on the intended publication such as name, place, and date of conference, periodical or journal title, or book title and publisher.)  |  |  |  |
| <b>II. AVAILABILITY CATEGORY</b><br>Check the appropriate category(ies):<br>Security Classification: <input type="checkbox"/> Secret <input type="checkbox"/> Secret RD <input type="checkbox"/> Confidential <input type="checkbox"/> Confidential RD <input checked="" type="checkbox"/> Unclassified<br>Export Controlled Document: <input type="checkbox"/> Documents marked in this block must be routed to NASA Headquarters International Affairs Division for approval.<br>NASA Restricted Distribution Document: <input type="checkbox"/> ITAR <input type="checkbox"/> EAR<br>Document disclosing an invention: <input type="checkbox"/> FEDD <input type="checkbox"/> Limited Distribution <input type="checkbox"/> Special Conditions-See Section III<br>Documents marked in this block must be withheld from release until six months have elapsed after submission of the report, unless a different release date is established by the appropriate counsel. (See Section IX).<br>Publicly Available Document: <input checked="" type="checkbox"/> Publicly available documents must be unclassified and may not be export-controlled or restricted on published documents.<br>Conc: <u>EM01/1. G. Sturdivant</u> |  |  |  |
| <b>III. SPECIAL CONDITIONS</b><br>Check one or more of the applicable boxes in each of (a) and (b) as the basis for special restricted distribution if the "Special Conditions" box under NASA Restricted Distribution Document in Section II is checked. Guidelines are provided on reverse side of form.<br>a. This document contains:<br><input type="checkbox"/> Foreign government information<br><input type="checkbox"/> Other-Specify _____<br>b. Check one of the following limitations as appropriate:<br><input type="checkbox"/> NASA personnel and NASA contractors only<br><input type="checkbox"/> U.S. Government agencies and U.S. Government agency contractors only<br><input type="checkbox"/> NASA contractors and U.S. Government agencies only<br><input type="checkbox"/> U.S. Government agencies only<br><input type="checkbox"/> Available only with approval of issuing office.   |  |  |  |
| <b>IV. BLANKET RELEASE (OPTIONAL)</b><br>All documents issued under the following contract/grant/project number _____<br>Date _____<br>The blanket release authorization granted is: _____<br><input type="checkbox"/> Rescinded - Future documents must have individual availability authorizations.<br><input type="checkbox"/> Modified - Limitations for all documents processed in the STI system under the blanket release should be changed to conform to blocks as checked in Section II.   |  |  |  |
| <b>V. PROJECT OFFICER/TECHNICAL MONITOR</b><br>Typed Name of Project Officer/Technical Monitor: <u>Lawrence Smith</u><br>Office Code: <u>EM11</u><br>Signature: <u>[Signature]</u><br>Date: <u>7/29/93</u>  |  |  |  |
| <b>VI. PROGRAM OFFICE REVIEW</b><br>Transmitted to CASI by memo <input type="checkbox"/> Approved <input type="checkbox"/> Not Approved<br>Typed Name of Program Office Representative: _____<br>Program Office and Code: _____<br>Signature: _____<br>Date: _____  |  |  |  |
| <b>VII. INTERNATIONAL AFFAIRS DIVISION REVIEW</b><br><input type="checkbox"/> Open, domestic conference presentation approved.<br><input type="checkbox"/> Foreign publication/presentation approved.<br><input type="checkbox"/> Export controlled limitation is not applicable.<br><input type="checkbox"/> The following Export controlled limitation (ITAR/EAR) is assigned to this document: _____<br>International Affairs Div. Representative: _____<br>Title: _____<br>Date: _____  |  |  |  |
| <b>VIII. EXPIRATION OF REVIEW TIME</b><br>The document is being released in accordance with the availability category and limitation checked in Section II since no objection was received from the Program Office within 20 days of submission, as specified by NHB 2200.2, and approval by the International Affairs Division is not required.<br>Name & Title: _____<br>Office Code: _____<br>Date: _____<br>Note: This release procedure cannot be used with documents designated as Export Controlled Documents, conference presentations or foreign publications.   |  |  |  |
| <b>IX. DOCUMENTS DISCLOSING AN INVENTION</b><br>a. This document may be released on _____ Date<br>Installation Patent or Intellectual Property Counsel<br>b. The document was processed on _____ Date<br>NASA CASI<br>In accordance with Sections II and III as applicable.   |  |  |  |